Simulation of three-dimensional compressible decaying isotropic turbulence using a redesigned discrete unified gas kinetic scheme (EP)

(iD) **Tao Chen** (陈涛), **Xin Wen** (温鑫), (iD) **Lian-Ping Wang** (王连平), (iD) **Zhaoli Guo** (郭照立), (iD) **Jianchun Wang** (王建春), **and Shiyi Chen** (陈十一)

COLLECTIONS

EP   This paper was selected as an Editor's Pick

openaccess

View Online   Export Citation   CrossMark

ARTICLES YOU MAY BE INTERESTED IN

Time-variant prediction of flow over an airfoil using deep neural network
Physics of Fluids **32**, 123602 (2020); https://doi.org/10.1063/5.0022222

Nonlinear transport of rarefied Couette flows from low speed to high speed
Physics of Fluids **32**, 112021 (2020); https://doi.org/10.1063/5.0029680

Fluid–structure interaction of a flexible membrane wing at a fixed angle of attack
Physics of Fluids **32**, 127102 (2020); https://doi.org/10.1063/5.0029378
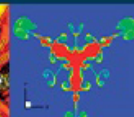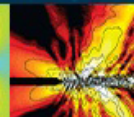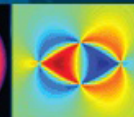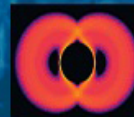
Physics of Fluids
GALLERY **OF COVERS**

AIP
Publishing

Simulation of three-dimensional compressible decaying isotropic turbulence using a redesigned discrete unified gas kinetic scheme ᴱᴾ

Tao Chen (陈涛),[1] 🔍ID Xin Wen (温鑫),[2] Lian-Ping Wang (王连平),[2,3,a] 🔍ID Zhaoli Guo (郭照立),[4] 🔍ID
Jianchun Wang (王建春),[3] 🔍ID and Shiyi Chen (陈十一)[1,3]

AFFILIATIONS

[1] State Key Laboratory for Turbulence and Complex Systems, College of Engineering, Peking University, Beijing 100871, China
[2] Department of Mechanical Engineering, 126 Spencer Laboratory, University of Delaware, Newark, Delaware 19716-3140, USA
[3] Guangdong Provincial Key Laboratory of Turbulence Research and Applications, Center for Complex Flows and Soft Matter Research and Department of Mechanics and Aerospace Engineering, Southern University of Science and Technology, Shenzhen 518055, Guangdong, China
[4] State Key Laboratory of Coal Combustion, School of Energy and Power Engineering, Huazhong University of Science and Technology, Wuhan 430074, Hubei, China

[a] Author to whom correspondence should be addressed: wanglp@sustech.edu.cn

ABSTRACT

In this paper, a new mesoscopic approach with both the adjustable Prandtl number and the ratio of bulk to shear viscosity has been developed to simulate three-dimensional compressible decaying homogeneous isotropic turbulence under the framework of discrete unified gas kinetic scheme (DUGKS). In the new approach, two reduced model Boltzmann equations with newly designed source terms are solved. In the continuum limit, the Navier–Stokes–Fourier system can be recovered by applying the Chapman–Enskog analysis. A three-dimensional DUGKS code has been developed, incorporating the fifth-order weighted essentially non-oscillatory scheme to better reconstruct the particle distribution functions at the cell interfaces. In addition, a new lattice velocity model with 77 discrete particle velocities is applied to ensure that the accuracy of the Gauss–Hermite quadrature is up to the ninth-order, and as such, the heat flux can be accurately evaluated. To validate our code, we simulate two cases with different initial turbulent Mach numbers and Taylor microscale Reynolds numbers. The simulation results converge with the increase in resolution and agree well with the results from the literature. As a direct application of our DUGKS, we briefly study the influence of bulk viscosity on turbulence statistics and flow structures. Our results show that the DUGKS is a reliable tool for simulating compressible decaying isotropic turbulence at low and moderate turbulent Mach numbers. More parametric studies are needed in the future to further explore the full capabilities of this specific mesoscopic method.

I. INTRODUCTION

Different flow regimes can be classified based on the Knudsen number (Kn), which is defined as the ratio of the microscopic mean free path of the particles λ and hydrodynamic length scale l. In terms of Kn, four flow regimes are typically identified, namely, continuum flow regime ($Kn < 10^{-3}$), slip flow regime ($10^{-3} < Kn < 10^{-1}$),

transition flow regime ($10^{-1} < Kn < 10$), and free-molecular flow regime ($Kn > 10$).[1] Compared to the continuum flow regime where the non-equilibrium effects are small, the non-equilibrium effects become more and more important with the increase in the local Knudsen number. For some unsteady multiscale problems and certain applications, several flow regimes can coexist.[2,3] In general, the conventional Navier–Stokes–Fourier (NSF) equation-based solvers

only treat the continuum flows correctly and cannot handle local flow regimes with high non-equilibrium effects. In addition, it is not feasible to derive a simple system of closed partial differential equations such as NSF equations for flows with locally varying Kn numbers. On the other hand, conceptually, the Boltzmann equation can not only describe the continuum regime but can also deal with non-continuum flows. This is one of the reasons that motivated the developments of mesoscopic computational fluid dynamics (CFD) methods based on the Boltzmann equations during the last three decades.

There are mainly two numerical approaches to solve the Boltzmann equation. The first one is called the direct simulation Monte Carlo (DSMC) method,[4] which is mainly used to simulate high-speed rarefied gas flows. However, the particle transport and collision processes are decoupled in the DSMC method, which implies that the grid spacing and the time step should be smaller than the mean free path and the relaxation time (equal to the ratio of the shear viscosity to the hydrodynamic pressure), respectively. In the local regions of nearly continuum flow in a multiscale physical problem, the computational cost for DSMC will increase enormously. In addition, for flows with low speed and small temperature variation, the statistical noise in the DSMC method will be on the order of the flow variables and would thus contaminate the simulation results.[5] The second approach that is used to solve the Boltzmann equation is the Discrete Velocity Methods (DVMs).[6–8] Most DVMs are essentially single-scale methods with particle collision and transport processes decoupled, which leads to the requirement that the grid spacing and time step should also be restricted by the mean free path and the relaxation time. The well-known lattice Boltzmann method (LBM) can be viewed as a special type of the discrete velocity formulation. However, in the LBM, the particle transport and collision are properly coupled. The LBM is mainly used to simulate incompressible or weakly compressible continuum flows under the low Mach number approximation.[9–11]

Recently, a unified gas kinetic scheme (UGKS)[12–15] has been developed to simulate all Knudsen number flows. The UGKS solves the hydrodynamic equations and the Boltzmann equation simultaneously. The evolution of kinetic variables and the evolution of hydrodynamic variables are coupled through the collision term and the cell interface fluxes in the UGKS. The UGKS can be viewed as an extension of the gas kinetic scheme (GKS),[16] which is mainly used to simulate continuum flows. A kinetic scheme is an asymptotic preserving (AP)[17] scheme if (a) the time step is not restricted by the particle collision time in the continuum regime and (b) it can recover the limiting hydrodynamic equations in the continuum limit. In the UGKS, the particle transport and collision processes are coupled due to the implicit treatment of the collision term such that the time step is no longer limited by the relaxation time. The AP property makes the UGKS a true multiscale scheme for simulating different flow regimes.

Guo et al.[17,18] proposed another unified gas kinetic scheme, namely, the discrete unified gas kinetic scheme (DUGKS) by combining the advantages of LBM and UGKS. Compared to the UGKS, the DUGKS is a simpler multiscale kinetic method. In the UGKS, the reconstruction of the cell-interface particle distribution function is based on the analytical solution of the Boltzmann equation along the characteristic line. However, in the DUGKS, the flux across the cell interface is evaluated from the particle distribution

functions at the half time step, and the particle distribution functions are obtained by using the characteristic method instead of using the analytical solution used in the UGKS. In the DUGKS, the Boltzmann equation is solved using an accurate finite-volume formulation coupled tightly with the particle transport and collision processes. Thus, the time step in the DUGKS is not limited by the particle collision time for all Kn numbers. Compared to the LBMs, the DUGKS can more easily incorporate irregular meshes and incorporate different discrete velocity models as the space grid is no longer coupled with the lattice velocity set. In addition, the DUGKS can ensure a second-order accuracy in both space and time. Due to the need of the reconstruction of the particle distribution function, the DUGKS is slightly more dissipative but with a better numerical stability than the LBM. The DUGKS has been applied to simulate single-phase decaying homogeneous isotropic turbulence,[19] wall-bounded turbulent channel flow,[20] 3D lid-driven cavity flow,[21] microchannel gas flows,[22] and immiscible two-phase flows.[23,24] Liu et al.[25] combined the total energy double-distribution-function (TEDDF) model[26] with the DUGKS to simulate thermal compressible flows in all flow regimes. For compressible flows, the Cartesian discrete velocity space may require a much larger degree of freedoms, and a higher order of the quadrature may also be needed; these will influence the accuracy of hydrodynamic variables and numerical instability. Recently, Chen et al.[27] combined the unstructured discrete velocity space[28] with the DUGKS in 2D. The unstructured velocity mesh adjusts the density of discrete velocities according to the local relative magnitude of the distribution function in the velocity space. Although it may be hard to optimize, it is usually better than a uniform velocity mesh. However, the DUGKS has not yet been applied to simulate *three-dimensional* compressible turbulence.

Compressible turbulence is of fundamental importance to many natural and engineering applications, such as solar winds, high-temperature reactive flows, and design of aircrafts. With the development of computational techniques, direct numerical simulation (DNS) has been applied as an independent research tool to probe complex flow structures in both incompressible turbulence and compressible turbulence. For compressible flows, shocklets may develop randomly due to local compressibility, causing local discontinuities as the turbulent Mach number increases, which can be a great challenge to the DNS.

The previous relevant DNS studies of compressible turbulence are briefly summarized here. Samtaney et al.[29] studied the decaying compressible turbulence and shocklet statistics at the initial turbulent Mach numbers of $Ma_{t0} = 0.1$–0.5 and the Taylor–Reynolds number of $Re_{\lambda 0} = O(50$–$100)$ using a tenth-order compact finite difference scheme. A shocklet extraction algorithm is also developed to extract and quantify the shocklet statistics from the DNS data. Honein and Moin[30] presented a numerical scheme with high entropy conservation and numerical stability to simulate compressible isotropic turbulence at the turbulent Mach number of $Ma_{t0} = 0.3$. Frapolli et al.[31] overcame the low Mach-number limit of the traditional LBM and proposed an entropic lattice Boltzmann model (ELBM) to simulate compressible transonic and supersonic flows using a $D3Q7^3$ lattice velocity model with temperature-dependent weights. In their work, they first simulated the flow around a NACA0012 airfoil immersed in a supersonic flow at $Ma = 1.4$ and $Re = 3 \times 10^6$. Then, they considered two

compressible decaying homogeneous isotropic turbulence (CDHIT) cases ($Re_{\lambda 0} = 72$, $Ma_{t0} = 0.1$ and $Re_{\lambda 0} = 175$, $Ma_{t0} = 0.488$) to further validate the capability of the ELBM. Liao et al.[32] applied the GKS to simulate CDHIT at a Taylor microscale Reynolds number of $Re_{\lambda 0} = 72.0$ and the turbulent Mach number of $Ma_{t0} = 0.1$–0.6. They concluded that the GKS is adequate for the DNS of moderately compressible homogeneous isotropic turbulence as far as the low-order turbulence statistics are concerned. Subbareddy and Candler[33] simulated compressible isotropic turbulence using an implicit, low dissipation finite-volume scheme and studied the effect of the dissipative flux on the quality of the simulated flow. The dissipative flux term F_{diss} in their numerical formulation is designed to capture shocklets and is expressed as $F_{diss} = \alpha_{diss} D_f$, where D_f represents the standard shock capturing scheme and the coefficient α_{diss} is close to 0 in smooth regions and tends to 1 in shocklet regions. The shock detection switch suggested by Ducros et al.[34] was applied for α_{diss} based on the local velocity divergence and vorticity magnitudes. By comparing the results obtained with different values of α_{diss}, they showed that the result using the switch of Ducros et al. achieves better agreement with the filtered DNS data. Later on, Wang et al.[35] proposed a hybrid scheme with an optimal treatment between the shock regions and the smooth regions. The hybrid scheme utilizes a seventh-order weighted essentially non-oscillatory (WENO) scheme for the shocklet regions and an eigth-order compact central finite difference (FD) scheme for smooth regions. A novel numerical hyperviscosity treatment is added to improve numerical instability. They simulated both decaying turbulence ($Ma_{t0} = 0.56$ and $Re_{\lambda 0} = 72$) and forced turbulence ($Ma_t = 1.08$ and $Re_\lambda = 177$). They concluded that their scheme is essentially a direct numerical simulation for scales of the order of a few Kolmogorov scales and larger. The underlying assumption for the hybrid method is that the dynamics of turbulence is unaltered even when the shock thickness is made as large as the Kolmogorov scale. Liu et al.[36] improved the hybrid scheme to simulate compressible isotropic turbulence at both relatively high turbulent Mach numbers ($Ma_t = 0.8$–2.08) and Reynolds numbers ($Re_\lambda = 107$–200). Recently, Chen et al.[37] applied the hybrid scheme to study the effect of bulk viscosity on both forced homogeneous isotropic turbulence and homogeneous shear turbulence. Most recently, Cao et al.[38] proposed a high-order gas kinetic scheme (HGKS) to simulate supersonic CDHIT. Their simulation covers the moderate Reynold numbers ranging from 10 to 72 and the Mach numbers ranging from 0.5 to 1.2. They also investigated the turbulent Mach number effect and the Reynolds number effect on flow statistical quantities.

Two relevant comments can be made here in terms of DNS of compressible flows. From a physical standpoint, the local Knudsen number Kn may not be small when the local Mach number is high enough to induce local shocklets. In other words, the local flow state is not uniform in the continuum flow regime. Therefore, the NSF system may fail to describe all local non-equilibrium effects, while the DUGKS can capture the physics in all flow regimes. In the hypersonic argon flow past over a sphere, the local Mach number in the wake region can still reach around 1.5.[39] From a numerical perspective, the NSF system needs a low-order treatment to capture shocklets and, at the same time, high-order treatment to capture turbulence fluctuations. Furthermore, the NSF system handles waves related to the hydrodynamics, while the DUGKS, instead, handles movements of particles, not the waves directly. The

wave dynamics is obtained as the moments in the particle velocity space. We believe that the discontinuity at the particle level is much weaker than the discontinuity in hydrodynamics. For this reason, as a multiscale method, it may be stated that the DUGKS is not required to incorporate drastically different treatments for different flow regimes.

In this paper, we apply the DUGKS combined with a fifth-order WENO scheme[40–43] to simulate CDHIT. A newly designed BGK model is utilized, allowing the variation of both the Prandtl number and the ratio of bulk to shear viscosity. The NSF system can be recovered in the continuum limit by applying the Chapman–Enskog expansion.[44]

The rest of this paper is organized as follows. In Sec. II, the original BGK–Shakhov model is briefly summarized, and a new model with an adjustable Prandtl number and a viscosity ratio is introduced. Through the Chapman–Enskog analysis, the NSF system for compressible flows can be recovered, and the relevant dimensionless parameters are briefly summarized. In Sec. III, we present the implementation details of the DUGKS under our altered design. Important statistical quantities about the CDHIT are reviewed in Sec. IV. A three-dimensional DUGKS code is developed to simulate CDHIT, and the results are discussed in Sec. V. Two simulation cases are considered, and the results are carefully compared with the literature data to validate our approach. Different WENO schemes and interfacial treatments are also compared to examine the sensitivity of flow statistics on implementation details. Finally, we investigate the effect of bulk to shear viscosity ratio on the statistics of turbulence by using our DUGKS approach. Major conclusions are summarized in Sec. VII, along with some additional discussions. In Appendixes A–E, we include the details on Hermite polynomials and our newly designed novel $E_{3,77}^9$ discrete particle velocity model (Appendix A), Hermite expansion of the equilibrium, the implementation of the fifth-order WENO scheme (Appendix B), the Chapman–Enskog analysis of our redesigned model (Appendix C), explicit expressions of two reduced distribution functions (Appendix D). The evolution equation of mean square velocity divergence is also derived in detail (Appendix E).

II. MESOSCOPIC MODELS

A. The BGK–Shakhov model

The Boltzmann equation with the BGK–Shakhov collision model[18,45] can be expressed as

$$\frac{\partial f}{\partial t} + \boldsymbol{\xi} \cdot \nabla f = \Omega_f \equiv \frac{f^S - f}{\tau}, \tag{1}$$

where $f(\boldsymbol{x}, \boldsymbol{\xi}, \boldsymbol{\eta}, \boldsymbol{\zeta}, t)$ is the particle distribution function, $\boldsymbol{x} = (x_1, \ldots, x_D)$ is the position, t is the time, $\boldsymbol{\xi} = (\xi_1, \ldots, \xi_D)$ is the particle velocity in D-dimensional space, $\boldsymbol{\eta} = (\eta_{D+1}, \ldots, \eta_3)$ is the particle velocity in the remaining $(3 - D)$ dimensional space, and $\boldsymbol{\zeta} = (\zeta_1, \ldots, \zeta_K)$ represents the K-dimensional internal degree of freedom. $\tau = \mu/p$ is the relaxation time and is related to the shear viscosity μ and pressure p, and $\nu = \mu/\rho$ is the kinematic viscosity.

By assuming that the particle motion in the (η, ζ) subspace is at local equilibrium, the Shakhov equilibrium distribution function is expressed as

$$f^S = f^{eq} + f^{Pr},$$

$$f^{eq} = \frac{\rho}{(2\pi RT)^{(3+K)/2}} \exp\left(-\frac{c^2 + \eta^2 + \zeta^2}{2RT}\right), \quad (2)$$

$$f^{Pr} = (1 - Pr)\frac{\boldsymbol{c} \cdot \boldsymbol{q}}{5pRT}\left(\frac{c^2 + \eta^2}{RT} - 5\right)f^{eq},$$

where f^{eq} is the Maxwellian distribution function, ρ is the density of fluid, R is the specific gas constant, T is the temperature, $\boldsymbol{c} = \boldsymbol{\xi} - \boldsymbol{u}$ is the particle thermal-fluctuation velocity with respect to the hydrodynamic velocity $\boldsymbol{u}$, Pr is the Prandtl number, and $\boldsymbol{q}$ is the heat flux. The extra term f^{Pr} is designed to adjust the heat flux and thus the Prandtl number. Without f^{Pr}, the Prandtl number would be 1. The equilibrium distribution implies that the ideal-gas equation of state (EOS), i.e., $p = \rho RT$, is satisfied.

The conservative variables are defined as the moments of the particle distribution function,

$$\rho = \int f d\boldsymbol{\xi} d\boldsymbol{\eta} d\boldsymbol{\zeta}, \quad \rho\boldsymbol{u} = \int \boldsymbol{\xi} f d\boldsymbol{\xi} d\boldsymbol{\eta} d\boldsymbol{\zeta},$$
$$\rho E = \frac{1}{2}\rho u^2 + \rho e = \int \frac{\xi^2 + \eta^2 + \zeta^2}{2}f d\boldsymbol{\xi} d\boldsymbol{\eta} d\boldsymbol{\zeta}. \quad (3)$$

Here, ρE is referred to as the total energy and $\rho e = \rho C_v T$ is the internal energy per unit volume. All relations in Eq. (3) remain valid if f is replaced by f^S.

With the above-mentioned equilibrium distribution, it can be shown that the specific heat capacity at constant volume C_v and that at constant pressure C_p are related to K and R as $C_v = (3 + K)R/2$ and $C_p = (5 + K)R/2$. Therefore, the specific heat ratio $\gamma = C_p/C_v = (5 + K)/(3 + K)$.

The viscous stress tensor σ and the heat flux $\boldsymbol{q}$ are determined by

$$\boldsymbol{\sigma} = -\int \boldsymbol{cc}(f - f^{eq})d\boldsymbol{\xi} d\boldsymbol{\eta} d\boldsymbol{\zeta}, \quad \boldsymbol{q} = \frac{1}{2}\int \boldsymbol{c}(c^2 + \eta^2 + \zeta^2)f d\boldsymbol{\xi} d\boldsymbol{\eta} d\boldsymbol{\zeta}. \quad (4)$$

The shear viscosity is determined by the intermolecular interactions and molecular thermal motions. For ideal gases, the shear viscosity increases with temperature, which introduces an additional effect of thermal field on the hydrodynamic velocity field. Two well-known models are widely used in the existing literature. The first one is called the hard-sphere (HS) or variable hard-sphere (VHS) model, which takes the form of power law.[2,29] The second one is known as the Sutherland's law,[46] which for air can be written as

$$\frac{\mu}{\mu_0} = \frac{1.4042(T/T_0)^{1.5}}{(T/T_0) + 0.404\,17}. \quad (5)$$

It has been verified from the experimental data that the HS model has a maximum relative error of about 5% for extreme cases of $T/T_0 \rightarrow 0.55$ and $T/T_0 \rightarrow 3$, while the Sutherland's law has a

maximum relative error of 2.0% at $T/T_0 = 3$ and less than 0.52% at $T/T_0 = 0.55$.[35] Therefore, the latter is used in our simulations.

The evolution of the particle distribution function depends only on the particle velocity in D-dimensional space. To reduce the computational cost, two reduced distribution functions residing in the lower dimensional phase-space [of dimension $(2D)$] are therefore introduced,[18]

$$g = \int f d\boldsymbol{\eta} d\boldsymbol{\zeta}, \quad h = \int (\eta^2 + \zeta^2)f d\boldsymbol{\eta} d\boldsymbol{\zeta}. \quad (6)$$

Thus, the evolution equation for g and h can be obtained from Eq. (1) to give

$$\frac{\partial g}{\partial t} + \boldsymbol{\xi} \cdot \nabla g = \Omega_g \equiv \frac{g^S - g}{\tau} = \frac{g^{eq} - g}{\tau} + \frac{g^{Pr}}{\tau}, \quad (7a)$$

$$\frac{\partial h}{\partial t} + \boldsymbol{\xi} \cdot \nabla h = \Omega_h \equiv \frac{h^S - h}{\tau} = \frac{h^{eq} - h}{\tau} + \frac{h^{Pr}}{\tau}, \quad (7b)$$

where the reduced Shakhov equilibrium functions are $g^S = g^{eq} + g^{Pr}$ and $h^S = h^{eq} + h^{Pr}$. g^{eq}, h^{eq} and g^{Pr}, h^{Pr} can be obtained by integrating f^{eq} and f^{Pr} over the (η, ζ) space, respectively.[18]

Two important observations are in order. The first concerns the computational cost of the model. Through the Chapman–Enskog analysis, we can observe that when using the BGK–Shakhov model, a Gauss–Hermite quadrature of up to the twelfth-order accuracy is needed to compute heat flux accurately as compared to the eigth-order accuracy without the Shakhov correction, which implies that, rigorously speaking, more discrete particle velocities should be used and that the computational cost will be increased. Therefore, an alternative model for a flexible Prandtl number will be considered instead. The second concerns the physical bulk viscosity in the model. It can be shown from the Chapman–Enskog expansion that the ratio between the bulk viscosity μ_V and the shear viscosity μ is $\chi \equiv \mu_V/\mu = 2/D - 2/(3 + K)$, which is always less than $2/D$. Therefore, for a fixed specific heat ratio, the original DUGKS cannot be used to investigate the physical effect of the bulk-to-shear viscosity ratio. Moreover, in the previous simulations done by using traditional CFD methods, the Stokes assumption with zero bulk viscosity is applied, and the specific heat ratio γ is equal to 1.4.[35] However, in the original DUGKS, setting the specific heat ratio $\gamma = 1.4$ means that the internal degree of freedom is $K = 2$. This will result in a non-zero bulk viscosity $\mu_V = 4\mu/15$. This difference in bulk viscosities in the BGK–Shakhov model and in the simulations reported in the literature makes precise inter-comparison impossible. To resolve these two issues together, we shall propose next a new model, which can have a flexible Prandtl number and an arbitrary ratio between bulk viscosity and shear viscosity; then, only a lattice velocity model with at least eigth-order quadrature accuracy is needed to correctly compute the heat flux, the highest order moment encountered in the Chapman–Enskog analysis for the NSF system.

B. A new model with adjustable Prandtl number and the ratio of bulk to shear viscosity

We shall begin with the same two reduced Boltzmann equations but instead with to-be-designed source terms S_g and S_h,

$$\frac{\partial g}{\partial t} + \boldsymbol{\xi} \cdot \nabla g = \frac{g^{eq} - g}{\tau} + S_g \equiv \Omega_g + S_g, \tag{8a}$$

$$\frac{\partial h}{\partial t} + \boldsymbol{\xi} \cdot \nabla h = \frac{h^{eq} - h}{\tau} + S_h \equiv \Omega_h + S_h, \tag{8b}$$

where the equilibrium distribution functions g^{eq} and h^{eq} are simply the Maxwellian

$$g^{eq} = \frac{\rho}{(2\pi RT)^{D/2}} \exp\left[-\frac{(\boldsymbol{\xi} - \boldsymbol{u})^2}{2RT}\right], \quad h^{eq} = (3 - D + K)RTg^{eq}. \tag{9}$$

The two source terms S_g and S_h are designed using an inverse design approach, as presented in Ref. 47. The design process is used to first find five integral constraints for the two source terms necessary to reproduce the NSF hydrodynamic system; then, a specific choice for S_g and S_h is derived based on the properties of the Hermite polynomials. The design is not unique. The results of our specific design, as explained in detail in Ref. 47, are

$$S_g = -\omega(\boldsymbol{\xi}, T_0)\left(\chi - \frac{2(3 - D + K)}{D(K + 3)}\right)\frac{p\vartheta}{2RT_0}\left(\frac{\xi^2}{RT_0} - D\right), \tag{10a}$$

$$S_h = \omega(\boldsymbol{\xi}, T_0)\left[\left(D - 2\frac{\boldsymbol{u} \cdot \boldsymbol{\xi}}{RT_0}\right)\left(\chi - \frac{2(3 - D + K)}{D(K + 3)}\right)p\vartheta \right.$$
$$\left. + \frac{2(1 - Pr)\boldsymbol{q} \cdot \boldsymbol{\xi}}{\tau RT_0}\right], \tag{10b}$$

where the weighting function $\omega(\boldsymbol{\xi}, T_0)$ is $\omega(\boldsymbol{\xi}, T_0) = \exp(-\xi^2/(2RT_0))/(2\pi RT_0)^{D/2}$, $\vartheta \equiv \nabla \cdot \boldsymbol{u}$ is the velocity divergence (dilatation), and T_0 is the reference temperature (see Appendix A for details). The velocity divergence is evaluated by either a second-order or fourth-order finite difference scheme for the present simulations, which can be further optimized.

The expressions for evaluating conservative variables, heat flux, and the viscous stress tensor are given as

$$\rho = \int g\,d\boldsymbol{\xi}, \quad \rho\boldsymbol{u} = \int \boldsymbol{\xi}g\,d\boldsymbol{\xi}, \quad \rho E = \frac{1}{2}\int (\xi^2 g + h)\,d\boldsymbol{\xi},$$
$$\boldsymbol{q} = \frac{1}{2}\int \boldsymbol{c}(c^2 g + h)\,d\boldsymbol{\xi}, \quad \boldsymbol{\sigma} = -\int \boldsymbol{cc}(g - g^{eq})\,d\boldsymbol{\xi}. \tag{11}$$

By using the Chapman–Enskog expansion, one can recover the following constitutive relation for the viscous stress tensor $\boldsymbol{\sigma}$:

$$\boldsymbol{\sigma} = 2\mu\left(\boldsymbol{S} - \frac{1}{D}\vartheta\boldsymbol{I}\right) + \mu_V\vartheta\boldsymbol{I} + \boldsymbol{O}(\tau^2), \tag{12}$$

where $\boldsymbol{S} = (\nabla\boldsymbol{u} + \nabla\boldsymbol{u}^T)/2$ is the strain rate tensor and $\boldsymbol{I}$ is the unit tensor. In addition, the closure model for heat flux vector $\boldsymbol{q}$ is consistent with Fourier's law,

$$\boldsymbol{q} = -\kappa\nabla T + \boldsymbol{O}(\tau^2), \tag{13}$$

where the thermal conductivity coefficient is $\kappa = \mu C_p/Pr$.

Applying the Chapman–Enskog analysis (see Appendix C), we can prove that the above-mentioned model can yield the following compressible Navier–Stokes–Fourier (NSF) system up to the order of $O(\tau)$:

$$\frac{\partial\rho}{\partial t} + \nabla \cdot (\rho\boldsymbol{u}) = 0, \tag{14a}$$

$$\frac{\partial(\rho\boldsymbol{u})}{\partial t} + \nabla \cdot (\rho\boldsymbol{uu}) = -\nabla p + \nabla \cdot \boldsymbol{\sigma}, \tag{14b}$$

$$\frac{\partial(\rho E)}{\partial t} + \nabla \cdot (\rho E\boldsymbol{u}) = -\nabla \cdot \boldsymbol{q} - \nabla \cdot (p\boldsymbol{u}) + \nabla \cdot (\boldsymbol{\sigma} \cdot \boldsymbol{u}). \tag{14c}$$

The following characteristic scales[35] are chosen to non-dimensionalize the above-mentioned NSF system. We choose a reference length scale L_0, reference velocity scale U_0, reference time scale L_0/U_0, reference temperature T_0, reference density ρ_0, reference speed of the sound $c_0 = \sqrt{\gamma RT_0}$, reference energy per unit volume $\rho_0 U^2$, reference pressure $p_0 = \rho_0 c_0^2/\gamma = \rho_0 RT_0$, reference viscosity μ_0, and reference thermal conductivity κ_0. Then, the dimension analysis shows that the system is governed by five dimensionless parameters: the Reynolds number $Re = \rho_0 UL/\mu_0$, Prandtl number $Pr = \mu_0 c_p/\kappa_0$, Mach number $Ma = U_0/c_0$, specific heat ratio γ (or internal degree of freedom K), and ratio between bulk viscosity and shear viscosity χ. If for a given fluid, γ, χ, and Pr are assumed to be known constants, the evolution of the system is then governed by two dimensionless parameters, i.e., the Reynolds number and the Mach number. For CDHIT, the initial flow Taylor microscale Reynolds number $Re_{\lambda 0}$ and the turbulent Mach number Ma_{t0}, along with the initial energy spectrum, are often used to describe the system.

III. THE DUGKS APPROACH

The implementation details about the DUGKS approach are described below. For convenience, we can rewrite the two Boltzmann equations in a unified form,

$$\frac{\partial\phi}{\partial t} + \boldsymbol{\xi} \cdot \nabla\phi = \Omega_\phi + S_\phi \equiv \bar{\Omega}_\phi, \tag{15}$$

where $\phi = g$ or h and the new collision operators are defined as $\bar{\Omega}_g \equiv \Omega_g + S_g$ and $\bar{\Omega}_h \equiv \Omega_h + S_h$.

As a finite-volume scheme, the computational domain is divided into many subcells V_j, with the cell centers denoted by $\boldsymbol{x}_j$. Integrating Eq. (15) over the control volume V_j from t_n to $t_{n+1}(=t_n + \Delta t)$ and using the midpoint rule for the integration of linear convective term and the trapezoidal rule for the combined collision operators, we can obtain

$$\tilde{\phi}_j^{n+1}(\boldsymbol{\xi}) = \tilde{\phi}_j^{+,n}(\boldsymbol{\xi}) - \frac{\Delta t}{|V_j|}J_\phi^{n+1/2}(\boldsymbol{\xi}), \tag{16}$$

where the flux across the cell interface at the half time step $(t_n + \Delta t/2)$ is

$$J_\phi^{n+1/2}(\boldsymbol{\xi}) = \oint_{\partial V_j} (\boldsymbol{\xi} \cdot \boldsymbol{n})\phi(\boldsymbol{x}, \boldsymbol{\xi}, t_{n+1/2})\,dS, \tag{17}$$

$|V_j|$ and ∂V_j denote the cell volume and the surface area of V_j, and $\boldsymbol{n}$ is the outward normal vector of the cell interface ∂V_j. $t_{n+1/2} = t_n + s$ represents the half time step with $s = \Delta t/2$. Two new distribution functions $\bar{\phi}$ and $\tilde{\phi}$ are introduced in order to convert the implicit time integration scheme to an explicit scheme, namely, $\bar{\phi} = \phi - (\Delta t/2)\bar{\Omega}_\phi$ and $\tilde{\phi}^+ = \phi + (\Delta t/2)\bar{\Omega}_\phi$. $\phi_j^n(\boldsymbol{\xi})$ and $\bar{\Omega}_{\phi,j}^n(\boldsymbol{\xi})$ are cell-averaged values of $\phi(\boldsymbol{x}, \boldsymbol{\xi}, t_n)$ and $\bar{\Omega}_\phi(\boldsymbol{x}, \boldsymbol{\xi}, t_n)$, respectively. In the implementation, we track the distribution function $\bar{\phi}$ instead of the original one.

Once the distribution function $\bar{\phi}$ is obtained, the conservative variables at the cell center can be computed as

$$\rho = \int \bar{g} d\boldsymbol{\xi}, \quad \rho\boldsymbol{u} = \int \boldsymbol{\xi}\bar{g} d\boldsymbol{\xi}, \quad \rho E = \frac{1}{2}\int (\xi^2 \bar{g} + \bar{h}) d\boldsymbol{\xi}. \tag{18}$$

In terms of the transformed distributions, the heat flux $\boldsymbol{q}$ and the viscous stress tensor $\boldsymbol{\sigma}$ at the cell center can be readily obtained as

$$\boldsymbol{q} = \frac{2\tau}{2\tau + \Delta t Pr}\frac{1}{2}\int \boldsymbol{c}(c^2\bar{g} + \bar{h})d\boldsymbol{\xi}, \tag{19}$$

$$\boldsymbol{\sigma} = -\frac{2\tau}{2\tau + \Delta t}\int \boldsymbol{cc}(\bar{g} - g^{eq})d\boldsymbol{\xi} + \frac{\tau\Delta t}{2\tau + \Delta t}\left(\chi - \frac{2(3 - D + K)}{D(3 + K)}\right)p\vartheta\boldsymbol{I}.$$

The surface flux integral at each interface is evaluated via the midpoint rule. In order to evaluate the flux term in Eq. (17) at the half time step, the original distribution function at the half time step is needed at the cell interfaces. This can be done by integrating Eq. (15) along the characteristic line for a half time step $s = \Delta t/2$ with the ending point located at the center of the cell interface $\boldsymbol{x}_b$. By using the trapezoidal rule for the collision term, we have

$$\phi(\boldsymbol{x}_b, \boldsymbol{\xi}, t_n + s) - \phi(\boldsymbol{x}_b - \boldsymbol{\xi}s, \boldsymbol{\xi}, t_n)$$
$$= \frac{s}{2}\left[\bar{\Omega}_\phi(\boldsymbol{x}_b, \boldsymbol{\xi}, t_n + s) + \bar{\Omega}_\phi(\boldsymbol{x}_b - \boldsymbol{\xi}s, \boldsymbol{\xi}, t_n)\right]. \tag{20}$$

Once again, two new transformed distribution functions $\bar{\phi} = \phi - (s/2)\bar{\Omega}_\phi$ and $\tilde{\phi}^+ = \phi + (s/2)\bar{\Omega}_\phi$ are introduced to remove the implicity. Then, we have $\bar{\phi}(\boldsymbol{x}_b, \boldsymbol{\xi}, t_n + s) = \tilde{\phi}^+(\boldsymbol{x}_b - \boldsymbol{\xi}s, \boldsymbol{\xi}, t_n)$. By applying the Taylor expansion, we can obtain

$$\bar{\phi}(\boldsymbol{x}_b, \boldsymbol{\xi}, t_n + s) = \tilde{\phi}^+(\boldsymbol{x}_b, \boldsymbol{\xi}, t_n) - \boldsymbol{\xi}s \cdot \boldsymbol{\sigma}_b, \tag{21}$$

where $\boldsymbol{\sigma}_b = \nabla\tilde{\phi}^+(\boldsymbol{x}_b, \boldsymbol{\xi}, t_n)$.

For compressible flows, the proper treatments of the local value $\tilde{\phi}^+(\boldsymbol{x}_b, \boldsymbol{\xi}, t_n)$ and local gradient $\boldsymbol{\sigma}_b$ are essential. First, we implement the fifth-order WENO-JS scheme[40] to reconstruct the distribution function $\tilde{\phi}^+(\boldsymbol{x}_b, \boldsymbol{\xi}, t_n)$ at the cell interface by using the cell-averaged values $\tilde{\phi}_j^n(\boldsymbol{\xi})$ and enforcing the upwind rule according to the direction of a given discrete particle velocity. The WENO-Z[41,42] and WENO-M[43] schemes are also tested, and the results are compared with those from the WENO-JS scheme. See Appendix B for more details of these reconstruction schemes. Second, we use van Leer limiter[48] to obtain the slope $\boldsymbol{\sigma}_j = \nabla\tilde{\phi}^+(\boldsymbol{x}_j, \boldsymbol{\xi}, t_n)$ at the cell center; then, it

follows that the gradient at the cell interface can be approximated by $\boldsymbol{\sigma}_b = (\boldsymbol{\sigma}_j + \boldsymbol{\sigma}_{j+1})/2$. An alternative way to evaluate the gradient $\boldsymbol{\sigma}_b$ is to use the finite difference schemes of different orders. To demonstrate the effect of different finite difference schemes used in the simulation, we will compare flow statistics from the second-order and the fourth-order central finite difference schemes in the second (higher Mach number) simulation case. If a shocklet is located near the cell interface, then $\boldsymbol{\sigma}_b$ could have a jump across the shocklet surface. In order to deal with this kind of discontinuity, $\boldsymbol{\sigma}_b$ is approximated by the gradient in the nearest upstream cell center or evaluated by the cell-averaged values in several upstream cells according to the direction of a given particle velocity. Finally, $\bar{\phi}(\boldsymbol{x}_b, \boldsymbol{\xi}, t_n + s)$ can be obtained according to Eq. (21).

In order to transform back to the original distributions, we first need to evaluate the conservative variables at the cell interface. They can be computed as

$$\rho(\boldsymbol{x}_b, t_n + s) = \int \bar{g} d\boldsymbol{\xi}, \quad \rho\boldsymbol{u}(\boldsymbol{x}_b, t_n + s) = \int \boldsymbol{\xi}\bar{g} d\boldsymbol{\xi},$$
$$\rho E(\boldsymbol{x}_b, t_n + s) = \frac{1}{2}\int (\xi^2 \bar{g} + \bar{h})d\boldsymbol{\xi}. \tag{22}$$

The heat flux can be evaluated by

$$\boldsymbol{q}(\boldsymbol{x}_b, t_n + s) = \frac{2\tau}{2\tau + sPr}\frac{1}{2}\int \boldsymbol{c}(c^2\bar{g} + \bar{h})d\boldsymbol{\xi}. \tag{23}$$

Therefore, the equilibrium distribution function $\phi^{eq}(\boldsymbol{x}_b, \boldsymbol{\xi}, t_n + s)$ can be computed based on the hydrodynamic variables obtained at the cell interface at the half time step. Then, the original distribution function can be obtained as

$$\phi(\boldsymbol{x}_b, \boldsymbol{\xi}, t_n + s) = \frac{2\tau}{2\tau + s}\bar{\phi}(\boldsymbol{x}_b, \boldsymbol{\xi}, t_n + s) + \frac{s}{2\tau + s}\phi^{eq}(\boldsymbol{x}_b, \boldsymbol{\xi}, t_n + s)$$
$$+ \frac{\tau s}{2\tau + s}S_\phi(\boldsymbol{x}_b, \boldsymbol{\xi}, t_n + s). \tag{24}$$

Finally, the flux across the cell interface $J_\phi^{n+1/2}(\boldsymbol{\xi})$ can be obtained by using Eq. (17).

Due to the nature of the linear transformation, the following two useful relations can be derived easily:

$$\tilde{\phi}^+ = \frac{4}{3}\bar{\phi}^+ - \frac{1}{3}\tilde{\phi}, \quad \bar{\phi}^+ = \frac{2\tau - s}{2\tau + \Delta t}\tilde{\phi} + \frac{3s}{2\tau + \Delta t}\phi^{eq} + \frac{3\tau s}{2\tau + \Delta t}S_\phi. \tag{25}$$

At last, the distribution function $\bar{\phi}$ can be updated through Eq. (16).

In the DUGKS, the time step is governed by the condition imposed on the Courant–Friedrichs–Lewy (CFL) number, $\Delta t = CFL \cdot \Delta x_{min}/(|\boldsymbol{u}|_{max} + |\boldsymbol{\xi}|_{max})$, where Δx_{min} is the minimal grid spacing, $|\boldsymbol{u}|_{max}$ is the local maximum hydrodynamic fluid velocity, and $|\boldsymbol{\xi}|_{max}$ is the local maximum discrete velocity. A new discrete particle velocity model ($E_{3,77}^9$) with 77 discrete particle velocities and ninth-order Gauss–Hermite quadrature has been used in the implementation. See Appendix A for details.

IV. PROBLEM DESCRIPTION OF COMPRESSIBLE DECAYING HOMOGENEOUS ISOTROPIC TURBULENCE (CDHIT)

The dynamic process is more complicated in a compressible turbulence than that in an incompressible turbulence, due to stronger coupling effects between the hydrodynamic flow quantities and thermodynamic quantities. With the increase in the turbulent Mach number, such coupling process will become increasingly stronger and finally leads to emergence of the shocklets.[35]

We consider CDHIT without an external driving force. The flow domain is a cubic box with the side length of $L = 2\pi$. The periodic boundary conditions and the uniform Cartesian grids are applied in all three directions. An initial divergence-free velocity field $\boldsymbol{u}(t = 0)$ is generated by a Gaussian random field with a prescribed kinetic energy spectrum $E(k, t = 0)$ in the spectral space. Then, the initial velocity field in the physical space is obtained by carrying out the inverse Fourier transformation. The initial kinetic energy spectrum is specified as[29]

$$E(k, t = 0) = A_0 k^4 \exp(-2k^2/k_0^2), \qquad (26)$$

where A_0 is the constant, k is the wavenumber, and k_0 is the peak wavenumber.

The relevant flow statistical quantities are summarized below. The root-mean-square velocity is defined as $u_{rms} = \langle \boldsymbol{u} \cdot \boldsymbol{u} \rangle^{1/2}/\sqrt{3}$, where the symbol $\langle \cdots \rangle$ denotes the spatial average over the whole domain at a given time. The Taylor microscale and Taylor microscale Reynolds numbers are defined as

$$\lambda = \frac{\sqrt{3} u_{rms}}{\langle (\partial u_1/\partial x_1)^2 + (\partial u_2/\partial x_2)^2 + (\partial u_3/\partial x_3)^2 \rangle^{1/2}},$$
$$Re_\lambda = \frac{u_{rms}\lambda\langle\rho\rangle}{\langle\mu\rangle}. \qquad (27)$$

The turbulent kinetic energy per unit mass and per unit volume is defined as

$$K(t) = \frac{1}{2}\langle \boldsymbol{u} \cdot \boldsymbol{u} \rangle = \int_0^\infty E(k, t)dk,$$
$$K_\rho(t) = \frac{1}{2}\langle \rho \boldsymbol{u} \cdot \boldsymbol{u} \rangle = \int_0^\infty E_\rho(k, t)dk, \qquad (28)$$

where $E(k, t)$ and $E_\rho(k, t)$ are the three-dimensional kinetic energy spectra corresponding to $K(t)$ and $K_\rho(t)$. The longitudinal integral length scale and the large eddy turnover time are given by

$$L_f = \frac{\pi}{2u_{rms}^2} \int_0^\infty \frac{E(k)}{k} dk, \; T_e = \frac{L_f}{u_{rms}}. \qquad (29)$$

The average viscous dissipation rate and the Kolmogorov length scale are defined as

$$\varepsilon = \left\langle \frac{1}{\rho}\boldsymbol{\sigma} : \boldsymbol{S} \right\rangle, \; \eta = \left[\frac{\langle \mu/\rho \rangle^3}{\varepsilon} \right]^{1/4}. \qquad (30)$$

The turbulent Mach number Ma_t and the local Mach number Ma_{loc} are, respectively, defined as

$$Ma_t = \frac{\langle u^2 \rangle^{1/2}}{\langle \sqrt{\gamma RT} \rangle}, \; Ma_{loc} = \frac{(\boldsymbol{u} \cdot \boldsymbol{u})^{1/2}}{\sqrt{\gamma RT}}. \qquad (31)$$

The root mean square dilatation, an important property for compressible flow, is defined as

$$\vartheta_{rms} \equiv \langle \vartheta^2 \rangle^{1/2} = \langle (\nabla \cdot \boldsymbol{u})^2 \rangle^{1/2}. \qquad (32)$$

In addition, the skewness and flatness of the longitudinal velocity derivatives are

$$S_u = \frac{\langle [(\partial u_x/\partial x)^3 + (\partial u_y/\partial y)^3 + (\partial u_z/\partial z)^3]/3 \rangle}{\langle [(\partial u_x/\partial x)^2 + (\partial u_y/\partial y)^2 + (\partial u_z/\partial z)^2]/3 \rangle^{3/2}}, \qquad (33)$$

$$F_u = \frac{\langle [(\partial u_x/\partial x)^4 + (\partial u_y/\partial y)^4 + (\partial u_z/\partial z)^4]/3 \rangle}{\langle [(\partial u_x/\partial x)^2 + (\partial u_y/\partial y)^2 + (\partial u_z/\partial z)^2]/3 \rangle^2}, \qquad (34)$$

where the velocity derivatives are evaluated by first transforming the velocity field into the spectral space, performing the gradient operations, and then transforming back to the physical space using the inverse Fourier transform.

In our simulation, the initial density ρ_0, pressure p_0, and temperature T_0 are set as constants. The initial turbulent kinetic energy K_0, the root mean square velocity u_{rms0}, dissipation rate ε_0, Kolmogorov length scale η_0, integral length scale L_{f0}, and large eddy turnover time Te_0 can be derived from the initial energy spectrum to give

$$K_0 = \frac{3A_0}{64}\sqrt{2\pi}k_0^5,$$
$$u_{rms0} = \left(\frac{2K_0}{3} \right)^{1/2}, \; \varepsilon_0 = 2\nu_0 \frac{15\sqrt{2\pi}}{256}A_0 k_0^7,$$
$$\eta_0 = \left(\frac{128\nu_0^2}{15\sqrt{2\pi}A_0 k_0^7} \right)^{1/4}, \; L_{f0} = \frac{\sqrt{2\pi}}{k_0}, \qquad (35)$$
$$Te_0 = \left(\frac{32}{A_0} \right)^{1/2}(2\pi)^{1/4}k_0^{-7/2}.$$

Therefore, the initial Taylor microscale Reynolds number $Re_{\lambda 0}$ and the initial turbulent Mach number Ma_{t0} can be computed as

$$Re_{\lambda 0} = \frac{(2\pi)^{1/4}}{4\nu_0}\sqrt{2A_0}k_0^{3/2}, \; Ma_{t0} = \frac{\sqrt{3}u_{rms0}}{\sqrt{\gamma RT_0}}. \qquad (36)$$

The time will be normalized by the initial large eddy turnover time T_{e0}, and the subscript "0" of T_{e0} will be omitted in all the subsequent figures for simplicity.

V. SIMULATION RESULTS

A three-dimensional DUGKS code is developed to simulate CDHIT by using the newly developed mesoscopic model. To

validate our code and test its ability to simulate CDHIT with different initial turbulent Mach numbers and Taylor microscale Reynolds numbers, two cases are considered, and the simulation results are carefully compared with the literature data based on other methods.

A. The low turbulent Mach number case

A case with a relatively low initial turbulent Mach number and a low initial Reynolds number ($Ma_{t0} = 0.3$, $Re_{\lambda 0} = 30$) is first simulated to validate our three-dimensional DUGKS code. The bulk-to-shear

viscosity ratio is set as 0 or 4/15, and the specific heat ratio γ is 1.4. The constant A_0 of the prescribed spectrum is 3.74×10^{-4}, and the corresponding peak wave number is $k_0 = 4$. The turbulent kinetic energy $K(t)$ is normalized by its initial value K_0, and three quantities representing normalized root mean square thermodynamic fluctuations are defined as follows:

$$p' = \frac{p_{rms}}{\gamma p_0 Ma_{t0}^2}, \quad T' = \frac{T_{rms}}{(\gamma - 1)T_0 Ma_{t0}^2}, \quad V' = \frac{V_{rms}}{V_0 Ma_{t0}^2}, \quad (37)$$
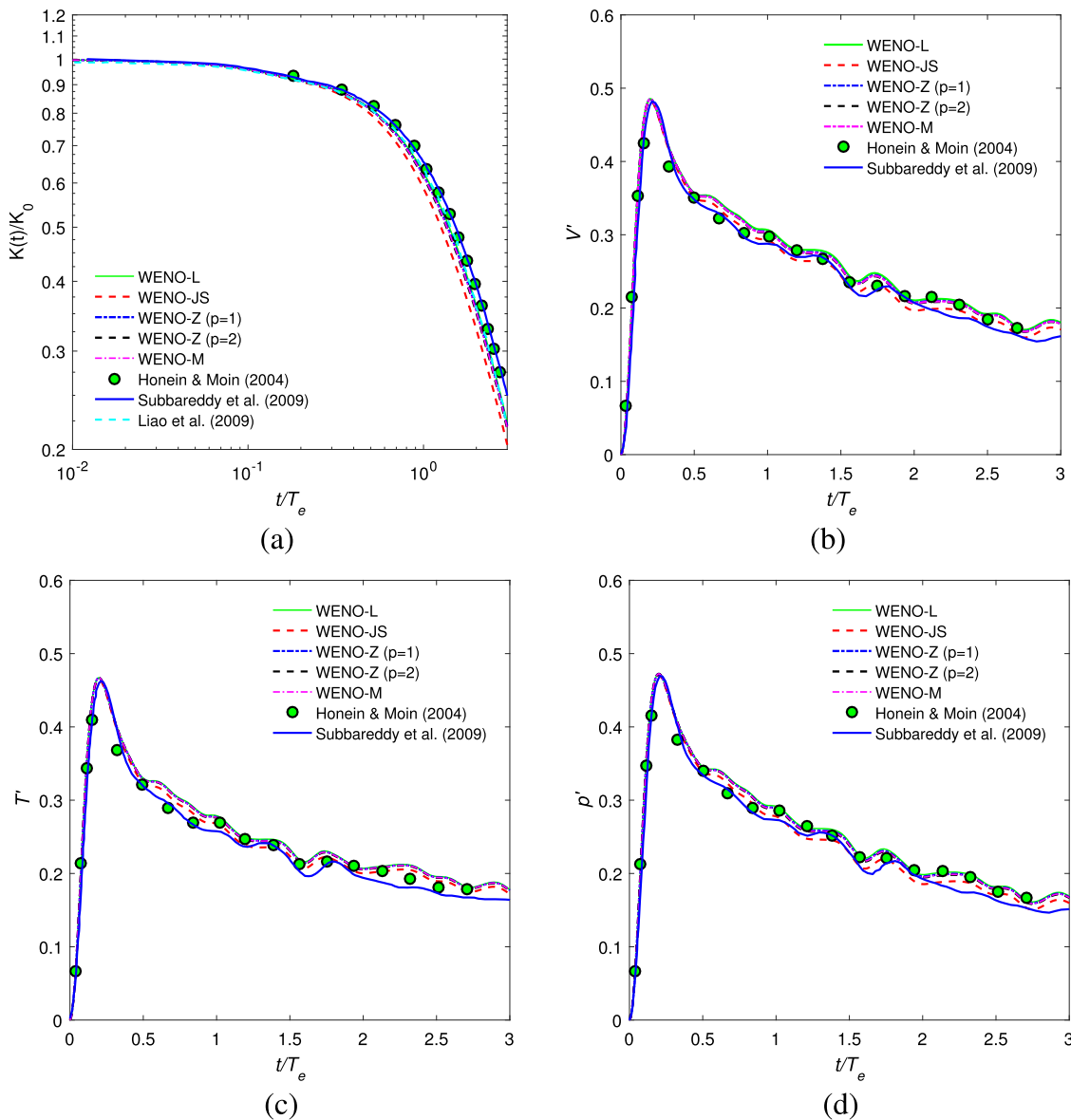
FIG. 1. Time evolution of (a) normalized turbulent kinetic energy $K(t)/K_0$, (b) normalized rms value of the specific volume V', (c) normalized rms value of the temperature T', and (d) normalized rms value of the pressure p', for the case of $Ma_{t0} = 0.3$ and $Re_{\lambda 0} = 30$.

where the specific volume of the fluid is defined as $V = 1/\rho$ and $V_0 = 1/\rho_0$. The physical quantity with a subscript rms denotes the root mean square value of the physical quantity. The CFL number is set to 0.5. In this case, the large eddy turnover time $T_e = 2\sqrt{3}/(k_0 M_{t0})$ in order to be consistent with the definition in the literature for the postprocessing.[30] The fifth-order WENO schemes are used to reconstruct the particle distribution functions at the cell interface.

First, several low resolution simulations are conducted. With 64^3 uniform grids as that used in the literature, Fig. 1 shows the results obtained by the DUGKS combined with different WENO schemes. The results of WENO-Z ($p = 1$) and WENO-Z ($p = 2$) almost overlap with those of WENO-M. The simulation results are compared to the data given by Honein and Moin,[30] Liao et al.,[32] and Subbareddy and Candler.[33] Overall, all DUGKS results match well with the literature data even at such a low resolution. The results obtained by the WENO-JS scheme are a little bit lower than other DUGKS results because WENO-JS is more dissipative than other WENO schemes. In contrast, the results obtained by Subbareddy and Candler.[33] are lower than other results for normalized thermodynamic fluctuation quantities after two large eddy turnover times.

Next, Fig. 2 shows the evolution of the velocity derivative skewness and flatness with 512^3 uniform grids. Their values approach almost a constant after one large eddy turnover time, indicating that the flow becomes physically developed. Then, the time evolution of normalized turbulent kinetic energy $K(t)/K_0$ and those normalized thermodynamic fluctuation quantities are carefully compared with the existing data from the literature in Fig. 3. Overall, the DUGKS results agree well with the reference data from the literature. We note that the reference results in the literature are obtained with only 64^3 uniform grid points, while the DUGKS results are obtained

with higher resolution. With the grid resolution 512^3, the results for thermodynamic fluctuation quantities almost overlap with those obtained by Honein and Moin[30] who used an entropy conservation sixth-order compact finite difference scheme. However, they do not provide enough data points in the peak region for comparison. Therefore, we do not know the exact position of the peak. It is observed that the peak position could be different when using different numerical treatments. For example, near the peak value of the curve, our results are almost identical with those obtained by Subbareddy and Candler[33] who used a low dissipation, finite-volume scheme. In contrast, the GKS results obtained by Liao et al.[32] are lower in the peak region. Moreover, the results obtained by different bulk-to-shear viscosity ratios only exhibit minor difference because the compressible effect is not so strong, and the difference in the bulk-to-shear viscosity ratio is not large enough in the present case. Still, we can see that the curve with $\chi = 4/15$ is a little bit lower than that with $\chi = 0$ for the thermodynamic flow quantity because a small increase in the bulk-to-shear viscosity ratio can decrease the compressibility effect slightly.

In the simulation of incompressible isotropic turbulence, Wang et al.[19] have shown that the DUGKS can resolve the flow when $k_{max}\eta > 3$ in their simulated cases, where k_{max} is the maximum wave number and η is the Kolmogorov length scale. However, for compressible isotropic turbulence, the approximate value for $k_{max}\eta$ is still unknown. The grid convergence study is done with the different uniform grids $N^3 = 64^3$, 128^3, 256^3, 512^3, and the simulation results are shown in Fig. 4. The corresponding initial values of $k_{max}\eta$ are 1.40, 2.88, 5.84, and 11.69, respectively. The DUGKS result with the lowest resolution 64^3 is reasonable but does not coincide very well with the reference data, especially for the kinetic energy. With the increase in the resolution, the results gradually converge to the data points given by Honein and Moin.[30] It is clear that the result with
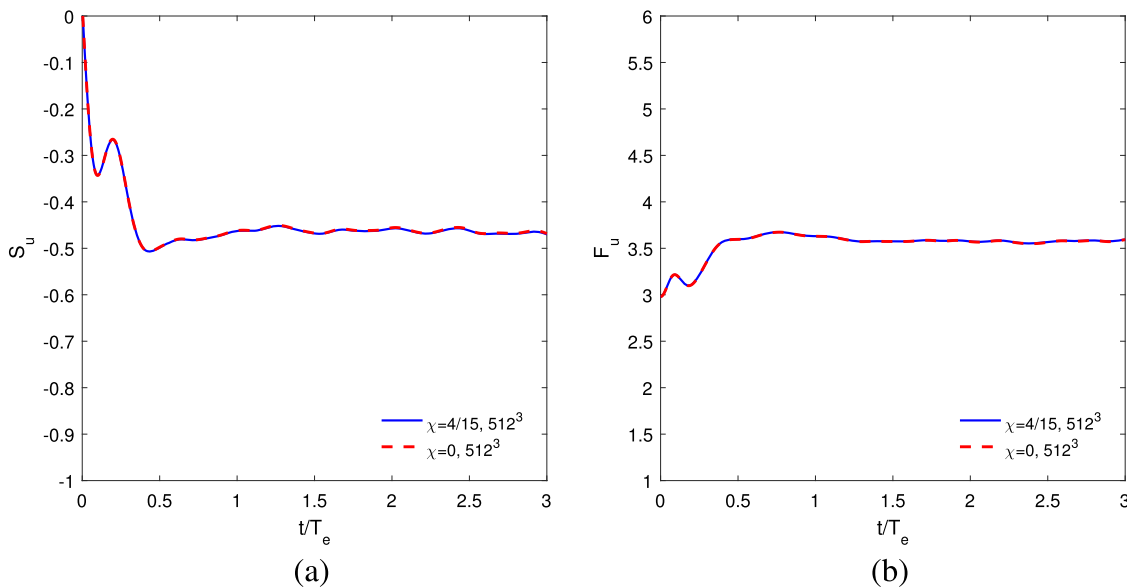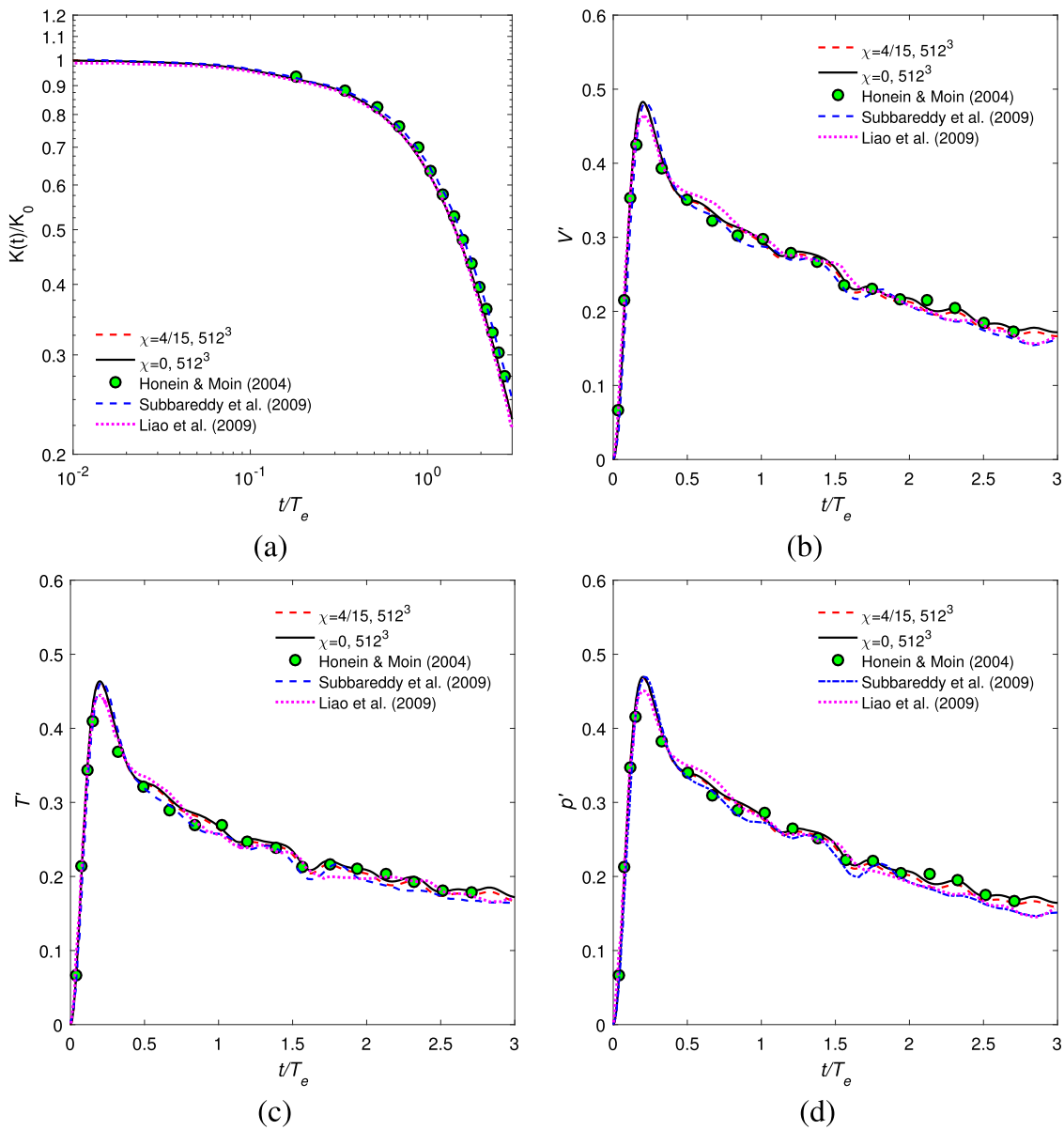

FIG. 2. Time evolution of (a) velocity derivative skewness S_u and (b) velocity derivative flatness F_u, for the case of $Ma_{t0} = 0.3$ and $Re_{\lambda 0} = 30$.
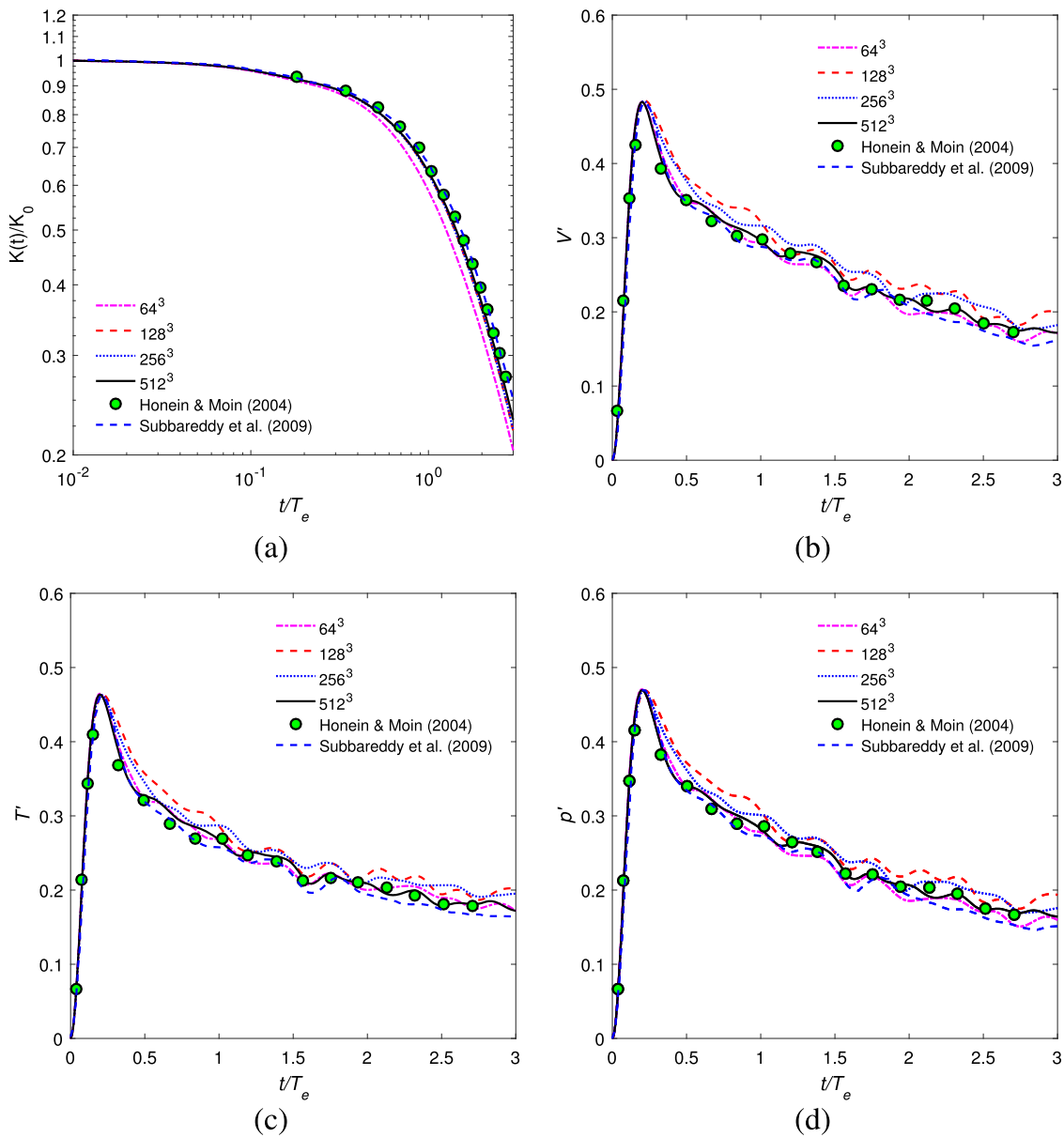
FIG. 3. Time evolution of (a) normalized turbulent kinetic energy $K(t)/K_0$, (b) normalized rms value of the specific volume V', (c) normalized rms value of the temperature T', and (d) normalized rms value of the pressure p', for the case of $Ma_{t0} = 0.3$ and $Re_{\lambda 0} = 30$.

highest resolution 512^3 is in good agreement with the data points in Ref. 30. Finally, the effect of the CFL number on the results is also examined for the present case. The bulk-to-shear viscosity ratio is 0. Three CFL numbers 0.25, 0.5 and 0.75 are tested on 512^3 uniform grid points. The time history of turbulent kinetic energy and the normalized pressure fluctuation are shown in Fig. 5. The results with different CFL numbers are almost identical. The explicit values $\Delta t/\tau_0$ ($\tau_0 = \mu_0/p_0$) for three CFL cases are 0.146, 0.292, and 0.437, respectively. This implies that accurate NSF solutions can be obtained

without the requirement that the time step should be much less than the relaxation time. This observation is consistent with the AP properties of the DUGKS approach.[18] Therefore, in all the subsequent sections, the CFL number is fixed at 0.5.

B. The higher turbulent Mach number case

To further validate the capability of the present DUGKS approach to simulate locally subsonic and supersonic turbulent

FIG. 4. Grid convergence study with uniform grids $N^3 = 64^3$, 128^3, 256^3, 512^3. (a) Normalized turbulent kinetic energy $K(t)/K_0$. (b) Normalized rms value of the specific volume V'. (c) Normalized rms value of the temperature T'. (d) Normalized rms value of the pressure p'. The bulk-to-shear viscosity ratio χ is set to 0. $Ma_{t0} = 0.3$ and $Re_{\lambda 0} = 30$.

flows, we consider a case with a higher initial turbulent Mach number of $Ma_{t0} = 0.488$ and a Taylor microscale Reynolds number of $Re_{\lambda 0} = 175$, previously studied by Samtaney *et al.*[29] and Frapolli *et al.*[31] The initial divergence-free velocity field is generated by an energy spectrum given in Eq. (26) with the constant of $A_0 = 0.011$ and the peak wavenumber of $k_0 = 4$. Two different grid resolutions, 256^3 and 512^3, are adopted for the newly developed mesoscopic model. The corresponding initial $k_{max}\eta_0$ are 2.43 and 4.89,

respectively. The CFL number is set to 0.5. The ratio of bulk to shear viscosity is 0 as in the simulations from the literature.

First, in Fig. 6, we display the time evolution of velocity derivative skewness and the root mean square value of velocity divergence. Results are compared with those from a NSF solver using a hybrid scheme[35] and the results from a tenth-order compact finite difference scheme.[29] Overall, our results are in good agreement with the literature data. Based on the time evolution of the velocity
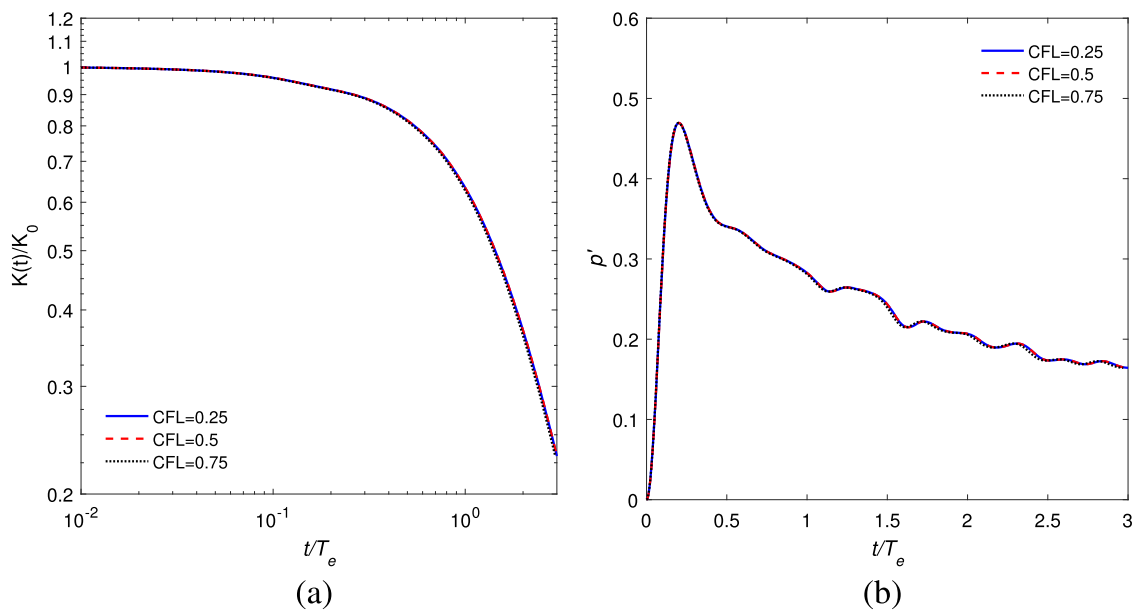
FIG. 5. Effect of time step size (or CFL number) of the results. Three CFL values (0.25, 0.5, and 0.75) were tested on uniform grids $N^3 = 512^3$. The bulk-to-shear viscosity ratio χ is 0. (a) Normalized turbulent kinetic energy $K(t)/K_0$. (b) Normalized rms value of the pressure p'. $Ma_{t0} = 0.3$ and $Re_{\lambda 0} = 30$.

derivative skewness, we conclude that the flow has not evolved into a physical flow before $t/T_e = 1.5$, during which the specific random flow initialization may affect the flow statistics. Different numerical treatments and grid resolutions will also introduce numerical dissipations at different levels, which can lead to the slight deviations near the peak and valley regions, but these regions occur during the transition from the initial random flow to the physical CDHIT flow. For these reasons, slight deviations at the regions near the peak and valley points for the skewness and the peak regions for the root mean square velocity divergence should not be
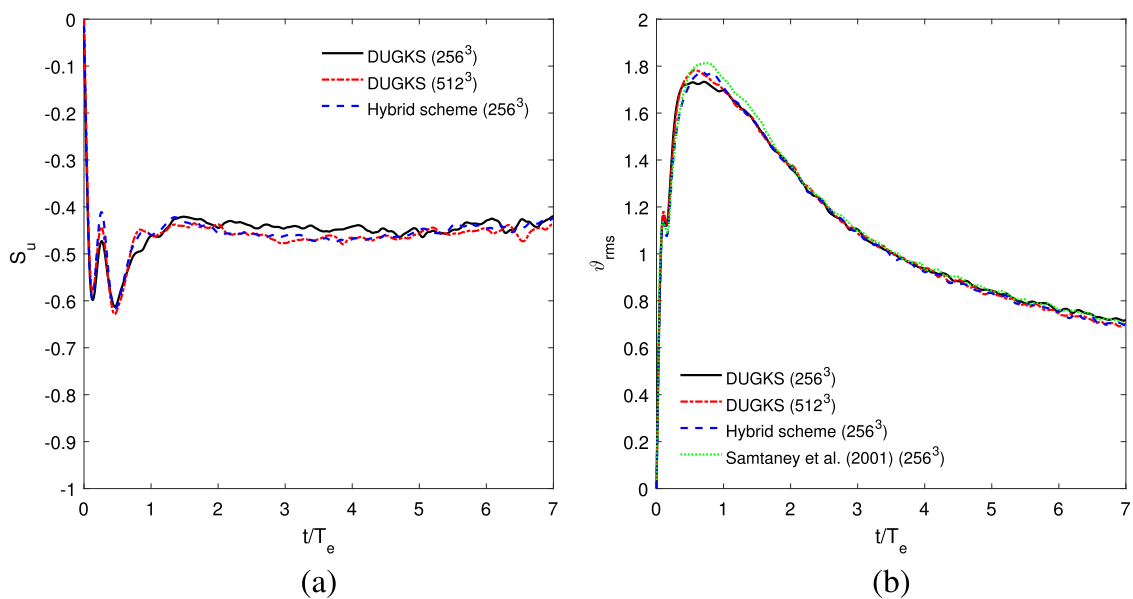
FIG. 6. (a) Time evolution of velocity derivative skewness S_u. (b) Time evolution of root mean square velocity divergence ϑ_{rms}.
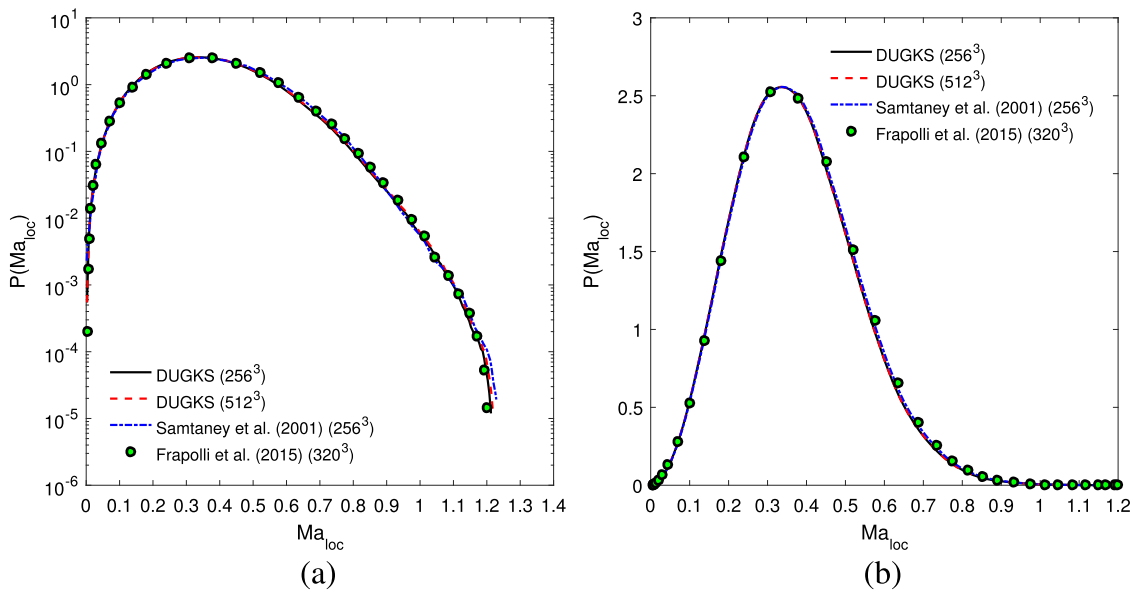
FIG. 7. Comparison of the PDF of the local Mach number at $t/T_e = 1.56$. (a) PDF with a logarithmic coordinate in the y axis. (b) PDF without logarithmic coordinates.

taken too seriously. The evolution of the $r$ms velocity divergence for $t/T_e > 1.5$ is in excellent agreement with the literature results. As illustrated in Fig. 6(b), even for the results between the work of Samtaney et al.[29] and Wang et al.,[35] some difference can be observed in the neighborhood of the peak value of the curves. In the following discussions, we will further confirm our statement here by simulating the same case with different WENO schemes and different treatments for interfacial derivatives of distribution functions at the cell interface.

Next, we compare the probability density function (PDF) of the local Mach number obtained by using the DUGKS approach with those obtained by Samtaney et al.[29] and Frapolli et al.[31] In Fig. 7, the DUGKS results and the benchmark data are compared with each other at the dimensionless time $t/T_e = 1.56$. We provide both the PDFs with and without the logarithmic y coordinate for comparison. In Fig. 7(a), we found that the DUGKS results agree very well with the benchmark data except for a minor difference in the region at the very end of the tail, perhaps due to the insufficient data samples. In Fig. 7(b), it is also observed that the DUGKS results overlap with the benchmark data for almost all Mach number regions.

A comparison of the PDF of normalized root mean square velocity divergence is shown in Fig. 8. We observe that the DUGKS results with 256^3 and 512^3 uniform girds are in excellent agreement with the data points taken from the work of Samtaney et al.[29] In contrast, the DUGKS result with 512^3 uniform grids exhibits a longer tail with large negative velocity divergence than that with 256^3 grids, although the probability of the large negative value is relatively small. The longer tail indicates that a high resolution simulation can better capture extreme turbulent fluctuations of different scales in local compression regions.

Figure 9 displays the PDF of the local Mach number and the PDF of normalized root mean square velocity divergence obtained

using the third-order WENO-JS scheme and the fifth-order WENO-JS scheme to reconstruct the particle distribution functions at the cell interface. Again, the DUGKS results are in good agreement with the benchmark data. In Fig. 9(a), only a slight deviation can be observed near the maximum Mach number. The results with the fifth-order WENO-JS scheme appear much closer to the benchmark data near the maximum Mach number when comparing with the third-order WENO-JS scheme. In Fig. 9(b), different treatments only show slight difference in the tails of the PDF. We choose to use the fifth-order WENO-JS scheme in the following simulations.
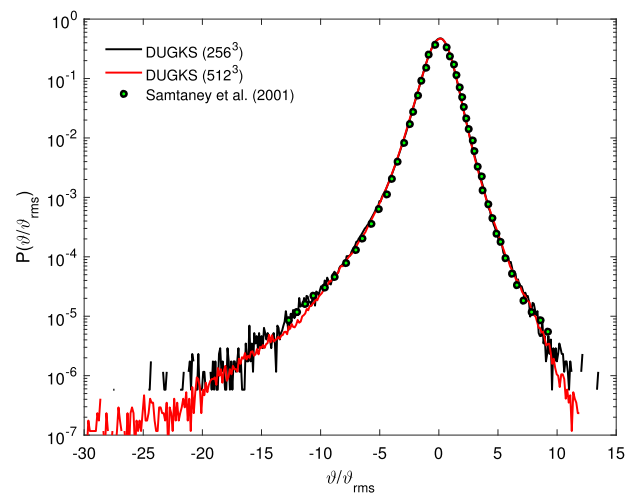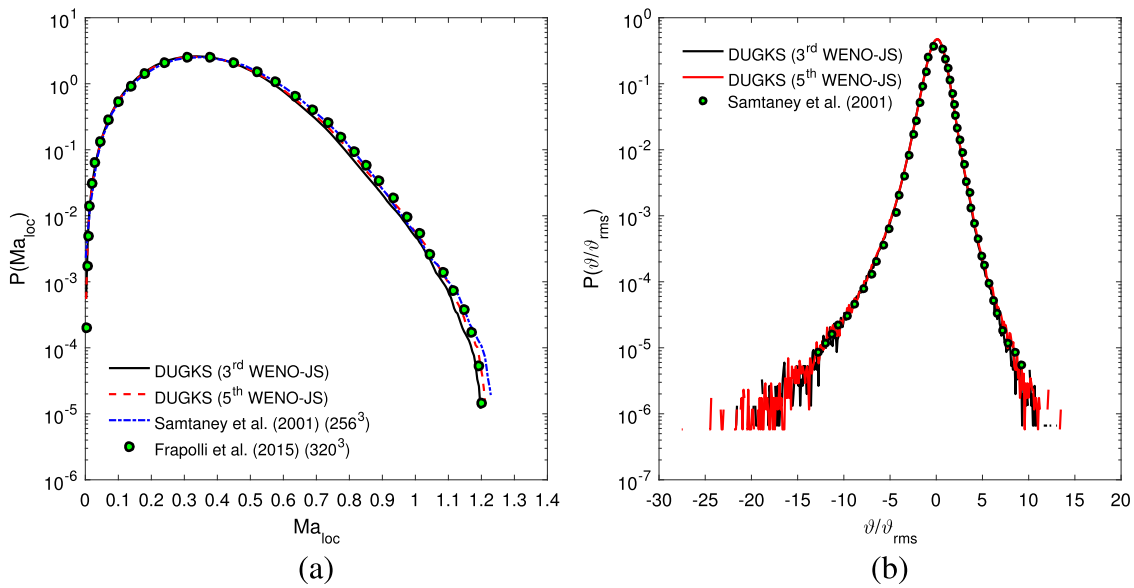

**FIG. 8**. Comparison of the PDF of normalized velocity divergence at $t/T_e = 1.56$.

FIG. 9. Comparison of the results obtained from the third-order WENO-JS scheme and the fifth-order WENO-JS scheme at t/T_e = 1.56. (a) PDF of the local Mach number. (b) PDF of the normalized velocity divergence.

To further validate our code, Fig. 10 shows the time history of the normalized turbulent Mach number and the normalized turbulent kinetic energy. The DUGKS results are in excellent agreement with the benchmark data. We also observe that the local maximum Mach number can reach values as high as 1.5, which is consistent with the observation reported by Frapolli et al.[31]

It would be interesting to examine the distribution of the local Knudsen number, $Kn \equiv \lambda/l$, where λ is the molecular mean free path and l is the local characteristic length scale. The value of l could be defined based on a hydrodynamic field variable, so the choice is not unique. Although the local Knudsen number can have different values due to different definitions of l, the following
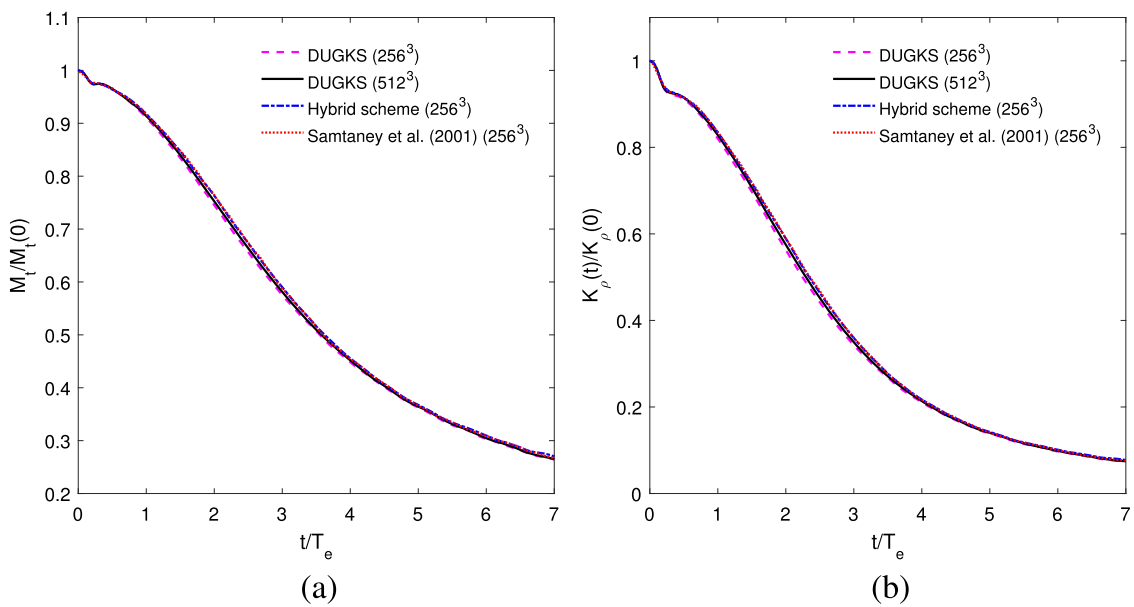
FIG. 10. (a) Time evolution of the turbulent Mach number Ma_t/Ma_{t0}. (b) Time evolution of normalized turbulent kinetic energy $K_\rho(t)/K_\rho(0)$.
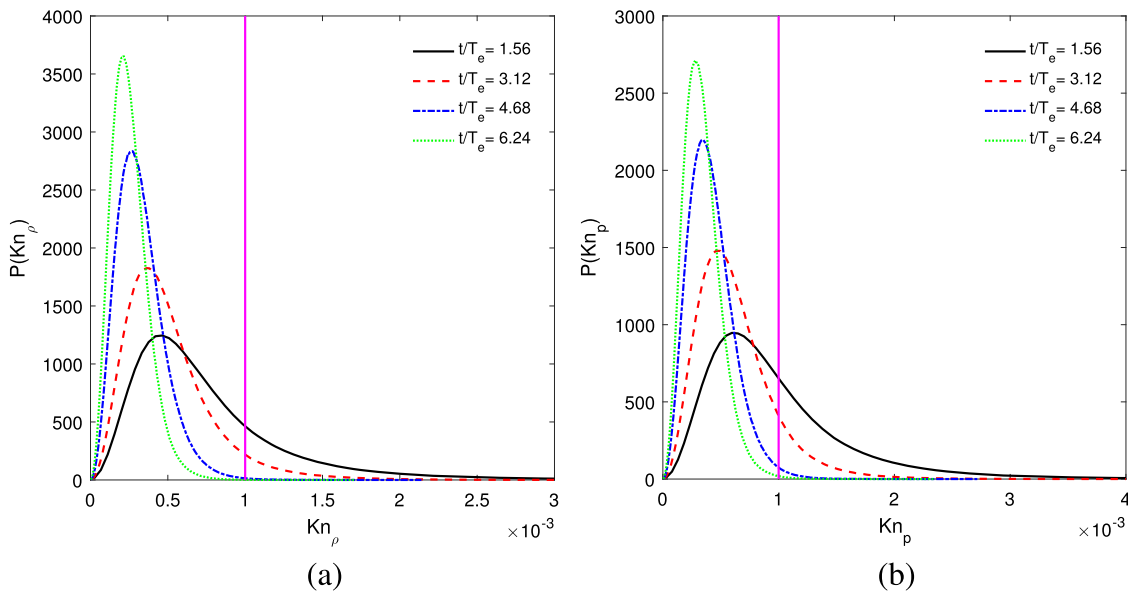
FIG. 11. (a) Time evolution of the PDF of the density-based Knudsen number Kn_ρ. (b) Time evolution of the PDF of the pressure-based Knudsen number Kn_p.

discussion can provide us a better understanding of the local flow state. Based on the density field and the temperature field, we can define three local Knudsen numbers, namely, $Kn_\rho \equiv \lambda |\nabla \rho|/\rho$, $Kn_{press} \equiv \lambda |\nabla p|/p$, and $Kn_T \equiv \lambda |\nabla T|/T$, where the mean free path is given by $\lambda = (\mu/p)\sqrt{\pi RT/2}$ for air.[17,49]

The evolution of PDFs of Kn_ρ and Kn_p is shown in Fig. 11. The peak value of the PDF increases, and the corresponding Knudsen number decreases over time. As a result, the flow state appears to be within the continuum regime completely as the flow evolves with time. We observe that the local Knudsen number can be larger

than 0.001 at earlier times. In the region with a high local Knudsen number, the flow may not belong to the continuum flow regime so that the NSF system cannot provide a satisfying description to the local flow state, especially near or inside the shocklets. However, for most flow regions, the NSF system can be accurate such that the NSF-based solver and the Boltzmann-based solver can yield identical results.

Figure 12 shows two snapshots of contours of normalized velocity divergence $\vartheta/\vartheta_{rms}$ and local Mach number Ma_{loc} at $z/L = 0.502$ and $t/T_e = 1.56$. Figure 13 displays slices of contours of
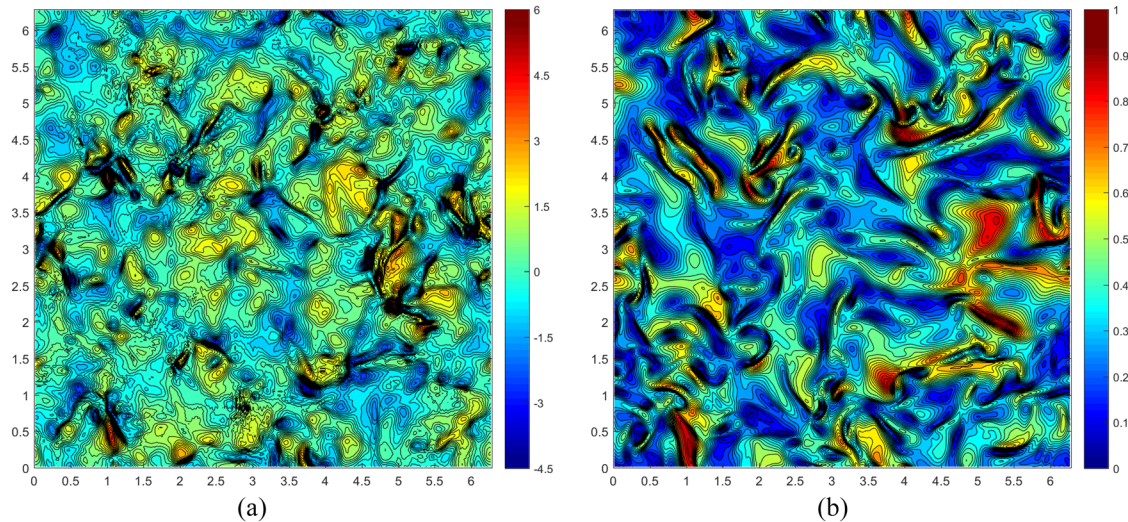

FIG. 12. Slices of contours of (a) normalized velocity divergence $\vartheta/\vartheta_{rms}$ and (b) local Mach number Ma_{loc} at $t/T_e = 1.56$.
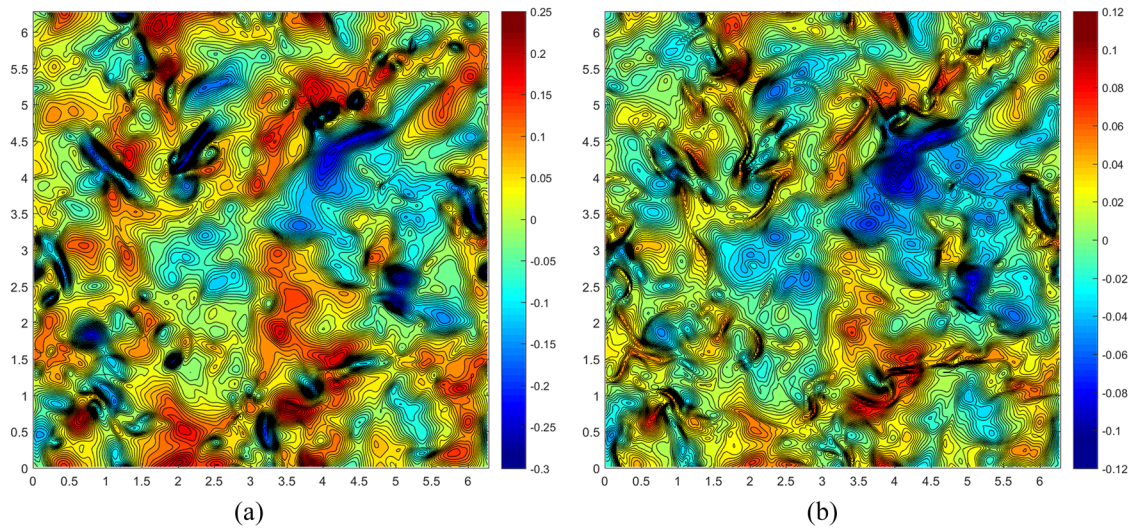
FIG. 13. Slices of contours of (a) normalized density fluctuation $(\rho - \langle \rho \rangle)/\langle \rho \rangle$ and (b) normalized temperature fluctuation $(T - \langle T \rangle)/\langle T \rangle$ at $t/T_e = 1.56$.

normalized density fluctuation $(\rho - \langle \rho \rangle)/\langle \rho \rangle$ and normalized temperature fluctuation $(T - \langle T \rangle)/\langle T \rangle$ at the same position and time. Local highly compression and expansion regions can be clearly observed in Figs. 13(a) and 13(b) which could be explained by the intermittency of compressible turbulence. The structures of the density fluctuations and the temperature fluctuations exhibit some similarities. Using the DNS data on this slice, we find that the correlation coefficient between the density fluctuation and the temperature fluctuation corr(ρ, T) is 0.90. For any two physical quantities ϕ and ψ, the correlation coefficient is defined as corr$(\phi, \psi) = \langle (\phi - \langle \phi \rangle)(\psi - \langle \psi \rangle) \rangle / \langle (\phi - \langle \phi \rangle)^2 \rangle^{1/2} \langle (\psi - \langle \psi \rangle)^2 \rangle^{1/2}$,

where the angle brackets denote spatial averages. Figure 14 displays the slices of contours of Kn_ρ and Kn_p at the same location and time. From Figs. 14(a) and 14(b) we observe that most flow regions reside in the continuum regime, while the regions with large density and pressure variations could reside in the slip regime locally. The correlation coefficient corr(Kn_ρ, Kn_p) is found to be 0.98, implying highly similar Knudsen number patterns displayed in Figs. 14(a) and 14(b). In addition, we find that corr$(Kn_\rho, |\nabla \rho|)$, corr$(Kn_\rho, |\nabla p|)$, corr$(Kn_p, |\nabla \rho|)$, and corr$(Kn_p, |\nabla p|)$ are 0.95, 0.94, 0.96, and 0.91, respectively. These relatively high levels of correlation confirm that large local Knudsen
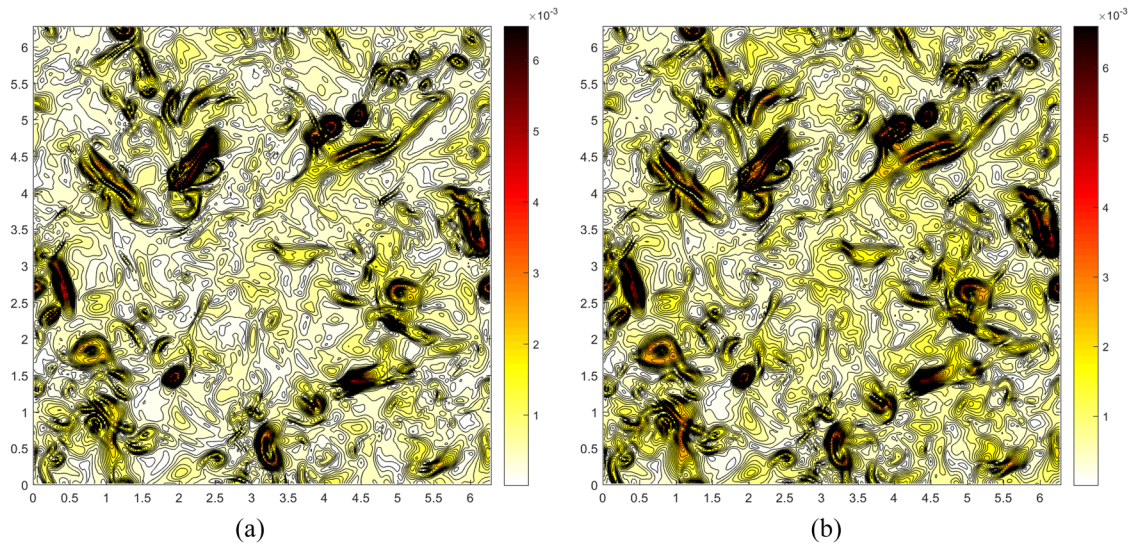

FIG. 14. Slices of contours of the (a) density-based local Knudsen number Kn_ρ and (b) pressure-based local Knudsen number Kn_p at $t/T_e = 1.56$.

numbers tend to overlap with regions of rapid density and pressure variations. Moreover, the correlation coefficients corr(Kn_ρ, ϑ^2), corr(Kn_ρ, Ma_{loc}), corr(Kn_p, ϑ^2), and corr(Kn_p, Ma_{loc}) are 0.24, 0.35, 0.27, and 0.37, respectively. We find that the quantities ϑ^2 and Ma_{loc} are all positively correlated with the local Knudsen numbers although the correlation coefficients are relatively small. These can be explained from two aspects. First, the negatively skewed PDF of the velocity divergence demonstrates that the very strong compression motions associated with the shocklets exist more frequently than the expansion motions in the whole flow field. Generally speaking, these strong compression motions could more effectively decrease the local length scale and thus increase the local Knudsen number. However, local expansion motions can also decrease the local density, increase the local density gradient, and thus increase the local Knudsen number, which is more pronounced when the expansion region is surrounded by some local compression regions (high density regions with negative velocity divergence). As clearly displayed in Figs. 12(a) and 13(a), the regions with a relatively high Knudsen number mainly correspond to the local low density regions induced by local strong expansion motions, but not by the local strong compression motions. Second, a rough estimate shows that the local Knudsen number is proportional to the ratio Ma_{loc}/Re_{loc}, where the local Reynolds number Re_{loc} is defined based on the local velocity scale and length scale. Therefore, local supersonic flow with a relatively large local Mach number may correspond to a relatively large local Knudsen number assuming that the local Reynolds number does not change significantly. In that case, a positive correlation between the local Mach number and the local Knudsen number can be observed. Based on these considerations, the Knudsen number patterns are related, at different levels, to the physical quantities shown in Figs. 12 and 13.

C. Comparison of different treatments of interfacial derivatives

In the simulations mentioned above, the interfacial distribution function $\bar{\phi}^+(\boldsymbol{x}_b, \boldsymbol{\xi}, t_n)$ is reconstructed from the cell-averaged value $\bar{\phi}_j^n(\boldsymbol{\xi})$ by applying the fifth-order WENO-JS scheme. Based on the known distribution functions $\bar{\phi}^+(\boldsymbol{x}_b, \boldsymbol{\xi}, t_n)$ and $\bar{\phi}_j^n(\boldsymbol{\xi})$, different numerical methods can be applied to evaluate the interfacial gradient $\boldsymbol{\sigma}_b$. In addition to the van leer limiter (method A) mentioned above, we also test the following the second-order (method B) and the fourth-order (method C) central finite difference schemes in our simulation. Note that for smooth flows without shocklets, $\boldsymbol{\sigma}_b$ should be continuous at the cell interface, while a jump of $\boldsymbol{\sigma}_b$ may occur across a strong shocklet surface in high turbulent Mach number flows. For the latter cases, the interfacial gradient $\boldsymbol{\sigma}_b$ can be approximated by the velocity gradient in the nearest upstream cell center obtained by using the van Leer limiter according to the direction of a given particle velocity (method D). The WENO-JS scheme and WENO-Z scheme are combined with methods A–D, respectively. The parameter p in the nonlinear weights of the WENO-Z scheme is equal to one. The grid resolution is 256^3.

For instance, we consider the implementation for the cell interfaces facing the x direction. In the normal direction of the cell interface, the second-order and fourth-order central FD schemes can be written as

$$\left(\frac{df}{dx}\right)_{i+1/2,j,k} = \frac{f_{i+1,j,k} - f_{i,j,k}}{\Delta x} + O(\Delta x^2), \tag{38a}$$

$$\left(\frac{df}{dx}\right)_{i+1/2,j,k} = \frac{27\left(f_{i+1,j,k} - f_{i,j,k}\right) - \left(f_{i+2,j,k} - f_{i-1,j,k}\right)}{24\Delta x} + O(\Delta x^4). \tag{38b}$$

In the tangential direction of the cell interface, the second-order and fourth-order central FD schemes can be expressed as

$$\left(\frac{df}{dy}\right)_{i+1/2,j,k} = \frac{f_{i+1/2,j+1,k} - f_{i+1/2,j-1,k}}{2\Delta y} + O(\Delta y^2), \tag{39a}$$

$$\left(\frac{df}{dz}\right)_{i+1/2,j,k} = \frac{f_{i+1/2,j,k+1} - f_{i+1/2,j,k-1}}{2\Delta z} + O(\Delta z^2), \tag{39b}$$

$$\left(\frac{df}{dy}\right)_{i+1/2,j,k} = \frac{8\left(f_{i+1/2,j+1,k} - f_{i+1/2,j-1,k}\right) - \left(f_{i+1/2,j+2,k} - f_{i+1/2,j-2,k}\right)}{12\Delta y}$$
$$+ O(\Delta y^4), \tag{39c}$$

$$\left(\frac{df}{dz}\right)_{i+1/2,j,k} = \frac{8\left(f_{i+1/2,j,k+1} - f_{i+1/2,j,k-1}\right) - \left(f_{i+1/2,j,k+2} - f_{i+1/2,j,k-2}\right)}{12\Delta z}$$
$$+ O(\Delta z^4), \tag{39d}$$

where the subscripts i, j, k denote the position of the function f and Δx, Δy, and Δz represent the grid spacings in x, y, z, respectively. All comparisons of methods A–D are performed at $t/T_e = 1.56$.

Figures 15 and 16 show the PDFs of the local Mach number and normalized velocity divergence. The results obtained from different methods are in good agreement with each other, and only small difference can be seen at the tails, which represent local highly compressed or expanded regions. Therefore, the PDFs of the local Mach number and normalized velocity divergence are not sensitive to the methods used to evaluate the interfacial gradient $\boldsymbol{\sigma}_b$.

Figures 17 and 18 display the time history of velocity derivative skewness and root mean square velocity divergence, respectively. As demonstrated in Fig. 17, the results obtained from methods A–D agree well with each other for both the WENO-JS and WENO-Z schemes, which indicates that the skewness is also not sensitive to the methods used. In Fig. 18(a), with the WENO-JS scheme, the DUGKS result from method A coincides well with the result from the hybrid scheme for most regions but has a lower peak value. In addition, the DUGKS results obtained from methods B–D are slightly lower than that obtained from method A. However, in Fig. 18(b), with the WENO-Z scheme, the DUGKS results obtained from methods B and C agree well with the hybrid scheme except for the peak region of the curve. In contrast, the DUGKS results obtained from methods A and D have a slightly higher value than that from the hybrid scheme for most regions but can reach the same level in the peak region. For this 3D compressible case, no analytical solution can be derived, and the truth benchmark can never be known thoroughly. If the traditional and mesoscopic CFD methods yield comparable results, then we can have more confidence in our simulation results. Moreover, we compare the instantaneous density and temperature profiles (not shown here). The results obtained from different methods also match very
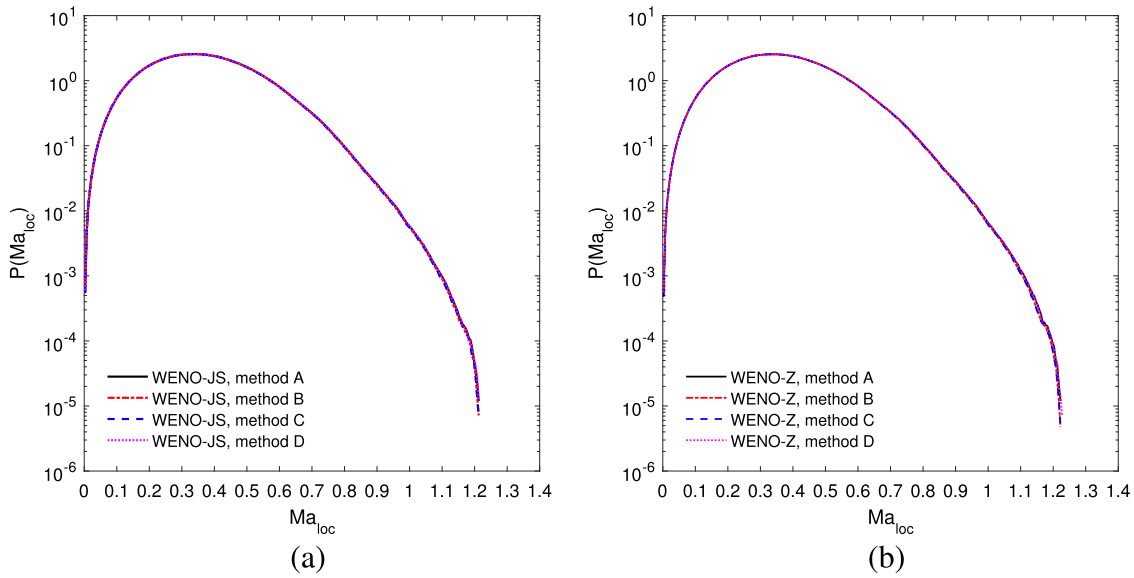
FIG. 15. Comparison of the PDF of the local Mach number by methods A–D at $t/T_e = 1.56$. (a) WENO-JS combined with methods A–D and (b) WENO-Z combined with methods A–D.

well with each other. From the above-mentioned results, we can conclude that different treatments at the cell interface can yield very similar results.

D. Comparison of different WENO schemes

In this subsection, we reconstruct the particle distribution functions at the cell interface by using WENO-JS, WENO-Z, and WENO-M schemes, respectively. The parameter p in the WENO-Z scheme is taken as 1 and 2 in the simulation. The details and some discussion on these three WENO schemes are included in Appendix C. As discussed above, method A is still used to compute σ_b at the cell interface. A 256^3 uniform grid is applied.

The PDFs of the local Mach number and normalized velocity divergence are plotted in Figs. 19(a) and 19(b). The DUGKS
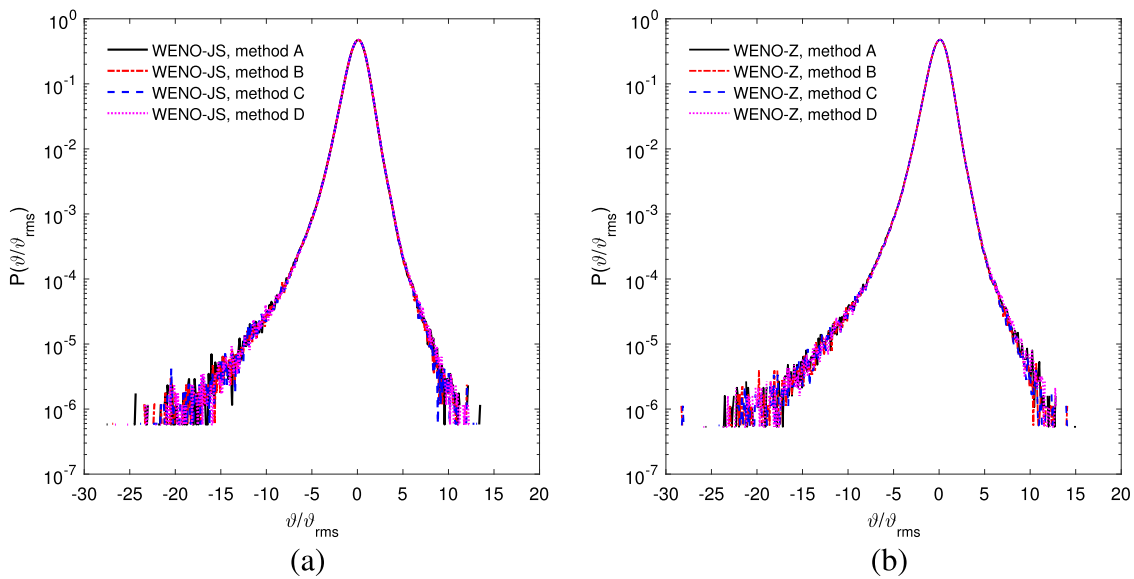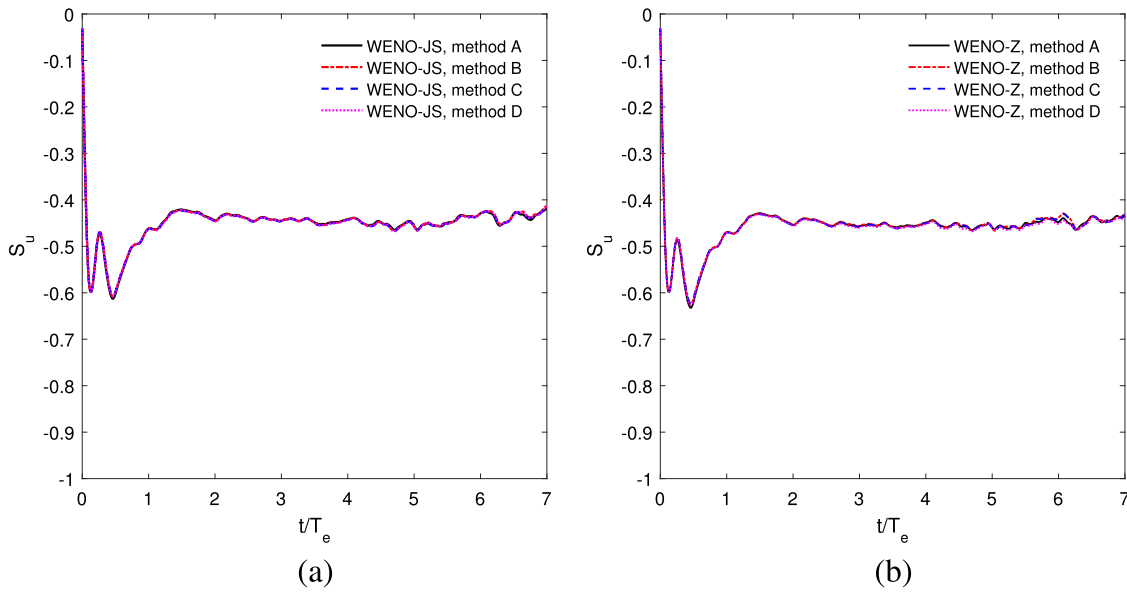

FIG. 16. Comparison of the PDF of normalized velocity divergence by using methods A–D at $t/T_e = 1.56$. (a) WENO-JS combined with methods A–D and (b) WENO-Z combined with methods A–D.

FIG. 17. Comparison of the time evolution of velocity derivative skewness by using methods *A–D*. (a) WENO-JS combined with methods *A–D* and (b) WENO-Z combined with methods *A–D*.

results obtained from different WENO schemes agree well with each other and the reference data. Figure 20(a) shows the evolution of velocity derivative skewness. Only small differences can be observed between these four curves. The evolution of root mean square velocity divergence is also shown in Fig. 20(b). The results obtained from

two WENO-Z schemes and WENO-M scheme are almost identical, but their magnitudes are slightly higher than those from the hybrid scheme and WENO-JS scheme for most regions although they share almost the same peak value. This is because the WENO-Z scheme and WENO-M scheme are more accurate and less dissipative than

FIG. 18. Comparison of the time evolution of root mean square velocity divergence by using methods *A–D*. (a) WENO-JS combined with methods *A–D* and (b) WENO-Z combined with methods *A–D*.

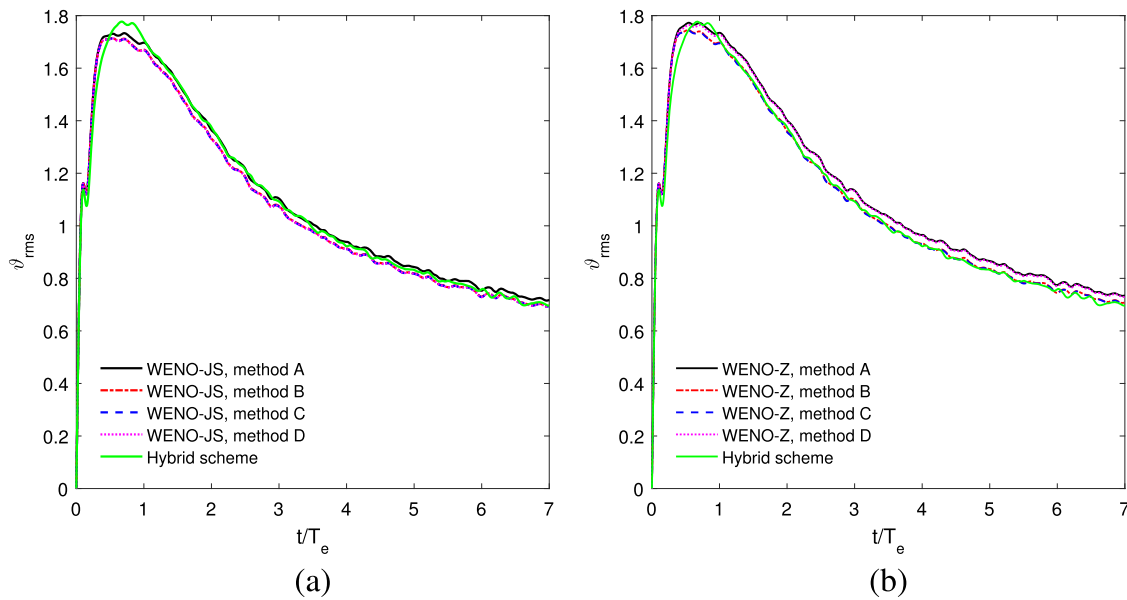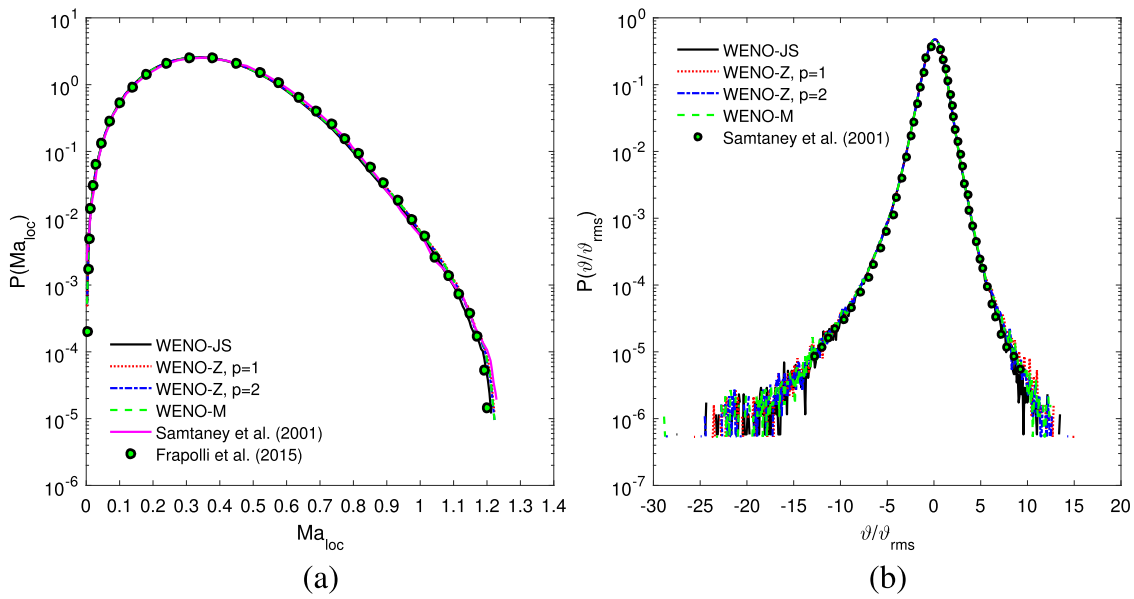**FIG. 19**. Comparison of the PDF of (a) the Mach number and (b) normalized velocity divergence by using different WENO schemes at t/T_e = 1.56.

the WENO-JS scheme, particularly near the critical points. We also confirm that the results do not show visible difference with the small parameter of $\varepsilon_0 = 10^{-5}$ and 10^{-6} (not shown here). The comparison leads to the conclusion that the PDFs of the local Mach number, normalized velocity divergence, and velocity derivative skewness are not very sensitive to the details of the WENO schemes applied. As to the

root mean square velocity divergence, the results are still reasonable. Different dissipation levels of different WENO schemes contribute to the small difference. We also compare the instantaneous density and temperature profiles (not shown here). No obvious difference could be observed, which implies that the instantaneous flow fields are also not sensitive to the WENO schemes applied.

FIG. 20. Comparison of the time evolution of (a) velocity derivative skewness and (b) root mean square velocity divergence by using different WENO schemes.

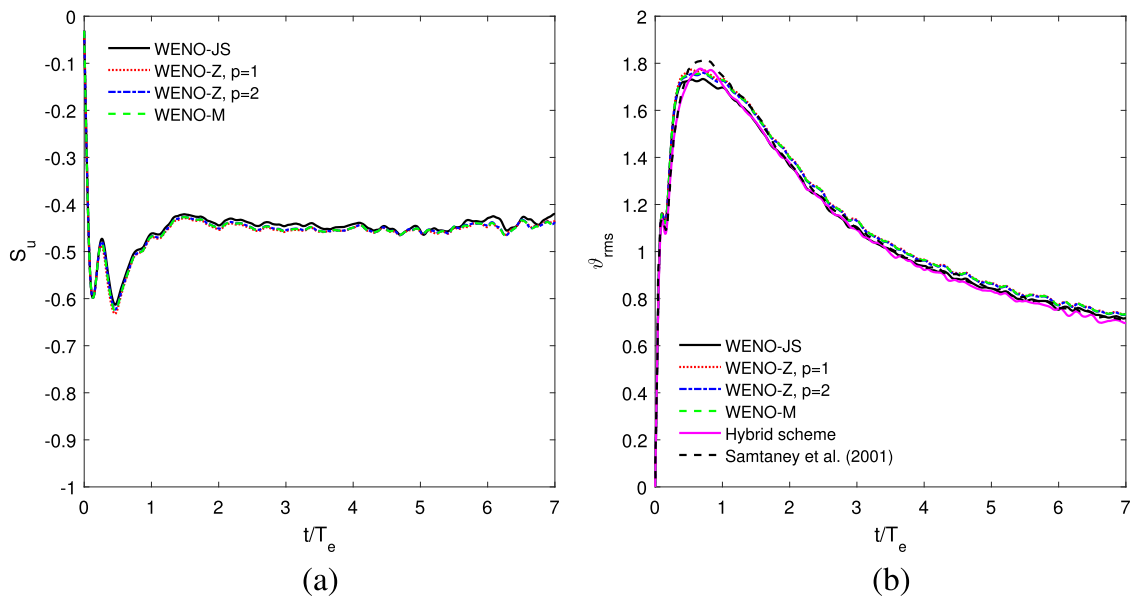### E. Effect of bulk to shear viscosity ratio on PDFs of some physical quantities

The Stokes hypothesis (i.e., zero bulk viscosity) is extensively applied to the NSF-based simulation of viscous compressible flows, in particular to gas dynamics problems.[29,35] The compressible turbulence is not expected to be affected by the bulk viscosity significantly when the bulk viscosity is of the order of the shear viscosity.[50] Therefore, the simulations with and without the Stokes assumption will yield almost the same results. As a direct application of our newly developed model, the effect of the bulk to shear viscosity ratio on PDFs of some physical quantities is explored by using our DNS data. Three viscosity ratios $\chi = 0$, 30, and 100 are considered, and some preliminary results are presented next.

First, the PDFs of normalized velocity divergence and local Mach number are shown in Figs. 21(a) and 21(b) at $t/T_e = 1.56$. When computing the PDFs, we first find the maximum (A_{max}) and minimum (A_{min}) values of the field; then, the bin width is defined as $(A_{max} - A_{min})/N_{bin}$. The number of bins, N_{bin}, is chosen to be 400. Oscillations of the PDF tails reflect the inadequate number of samples used there. As illustrated in Fig. 21(a), we observe that the left tail with large negative values becomes shorter with the increase in the bulk to shear viscosity ratio, which is qualitatively consistent with those reported by Chen *et al.*[37] and Pan and Johnsen.[50] This is because the increase in the bulk to shear viscosity ratio can damp the compressibility. In Fig. 21(b), the maximum Mach number also decreases with the increase in the bulk to shear viscosity ratio, which further confirms the previous observation. An explanation for the bulk viscosity effect is given as follows. For simplicity, neglecting the spatial variation of the shear and bulk viscosities in the viscous term, the spatially averaged evolution equation for $\langle \vartheta^2 \rangle /2$ in a periodic domain can be derived from the momentum equation, yielding

$$\frac{\partial}{\partial t}\left\langle \frac{1}{2}\vartheta^2 \right\rangle = \left\langle \frac{1}{2}\vartheta^3 \right\rangle + \langle \vartheta(\boldsymbol{\Omega} : \boldsymbol{\Omega} - \boldsymbol{S} : \boldsymbol{S}) \rangle$$
$$+ \left\langle \frac{1}{\rho}\nabla p \cdot \nabla \vartheta \right\rangle - \left\langle \frac{4}{3}\frac{\mu}{\rho}|\nabla\vartheta|^2 \right\rangle$$
$$- \left\langle \frac{\mu_V}{\rho}|\nabla\vartheta|^2 \right\rangle, \tag{40}$$

where the minus sign in the last term implies that the bulk viscosity always reduces the velocity divergence magnitude in both the expansion and compression regions. This equation can be used to further analyze different contributions to the change in the mean square dilatation, which is beyond the scope of this paper. The derivation details are included in Appendix E.

Next, Figs. 22(a) and 22(b) present the PDFs of normalized vorticity magnitude ω/ω_{rms} and the normalized vortex stretching term $\Phi = (\boldsymbol{\omega} \cdot \boldsymbol{S} \cdot \boldsymbol{\omega})/(\langle \omega^2 \rangle(\boldsymbol{S} : \boldsymbol{S})^{1/2})$ at $t/T_e = 1.56$. Different from the previous ones, it is found that the PDFs of normalized vorticity magnitude and the normalized vortex stretching term exhibit little sensitivity to the ratio of bulk to shear viscosity. The PDFs are almost identical for different bulk-to-shear viscosity. This is also consistent with the findings by Pan and Johnsen.[50] Another evidence can be found in Fig. 23 that displays the vortices extracted by Q-criterion[51] at $t/T_e = 1.56$ for $\chi = 0$, 30, respectively. We observe that the vortex structures are almost unaffected by the bulk-to-shear viscosity ratio. This can be understood from two aspects. On the one hand, the vorticity dynamics is dominated by the vortex stretching and shear-density gradient effects and could be partly influenced by the bulk viscosity-density gradient effect.[50] On the other hand, increasing the bulk-to-shear viscosity ratio can attenuate the coupling between the solenoidal mode and the compressive mode such that the
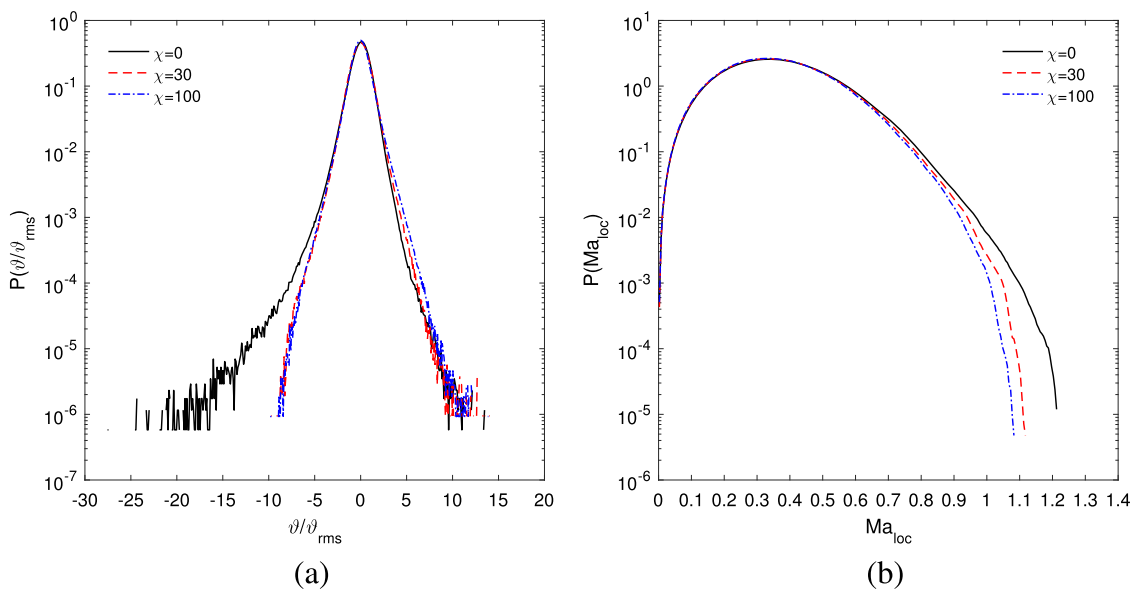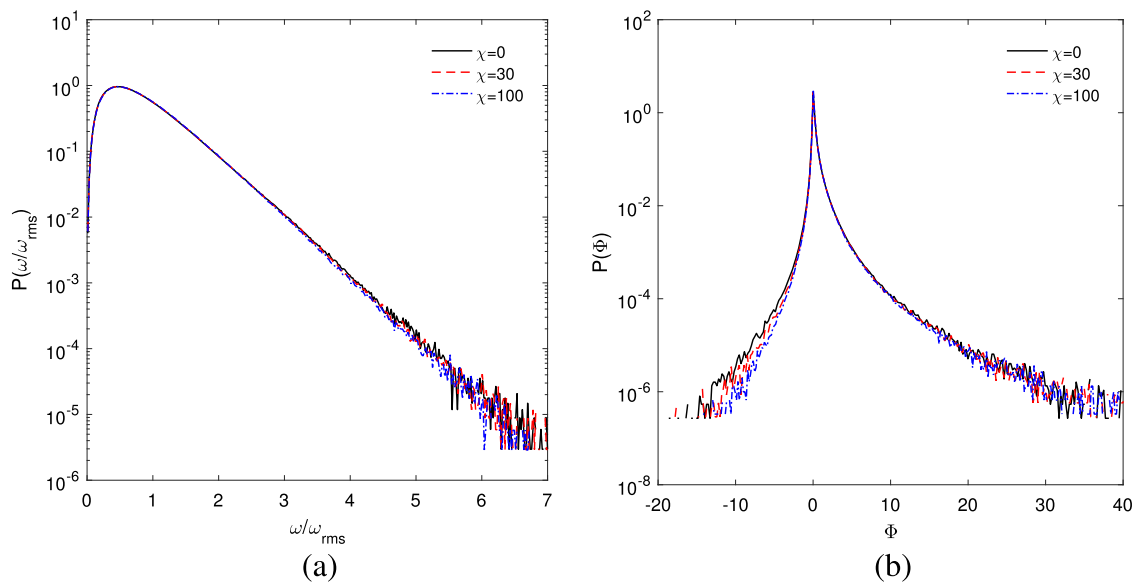

FIG. 21. (a) PDF of normalized velocity divergence $\vartheta/\vartheta_{rms}$. (b) PDF of the local Mach number Ma_{loc}. Time $t/T_e = 1.56$.

FIG. 22. (a) PDF of normalized vorticity magnitude ω/ω_{rms}. (b) PDF of normalized vortex stretching term $\Phi = (\boldsymbol{\omega} \cdot \boldsymbol{S} \cdot \boldsymbol{\omega})/(\langle \omega^2 \rangle \langle \boldsymbol{S}:\boldsymbol{S} \rangle^{1/2})$. Time $t/T_e = 1.56$.

solenoidal-velocity-dominated vortical motion is not evidently altered by the bulk viscosity.

To have an intuitive understanding of effect of the bulk to shear viscosity ratio, the isosurfaces of the normalized velocity divergence $\vartheta/\vartheta_{rms}$ with $\chi = 0, 30$ are also visualized in Figs. 24(a) and 24(b) at $t/T_e = 1.56$, respectively. The red isosurfaces ($\vartheta/\vartheta_{rms} = -2$) denote the compression regions, while the blue ones ($\vartheta/\vartheta_{rms} = 2$) represent the expansion regions. We observe that more blob-like structures emerge, and the sheet-like structures is less visible with the increase in the bulk to shear viscosity ratio. The increase in the bulk to shear viscosity ratio damps the compressible effect in the local strong compression regions and reduces the probability of the existence of the shocklets, which finally drives the flow toward the incompressible state.
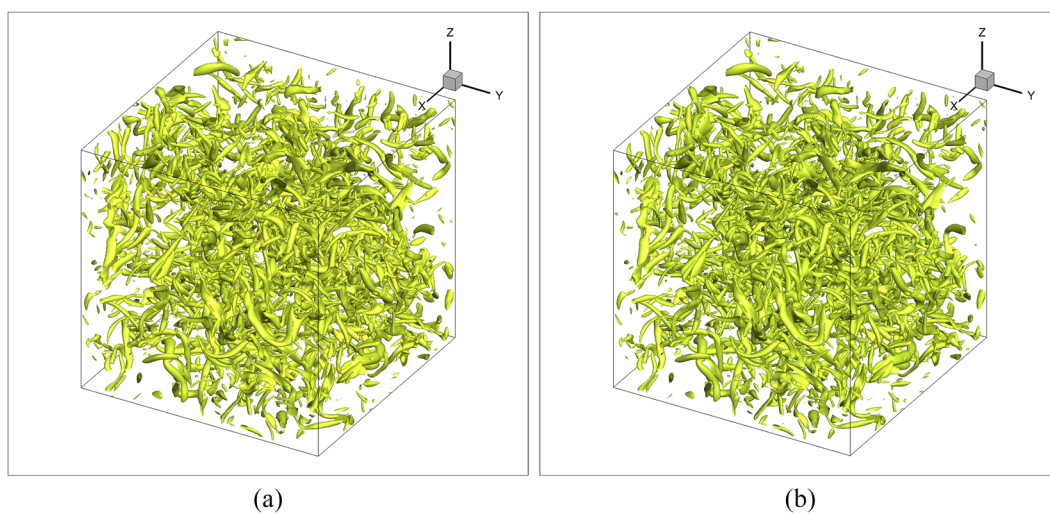
FIG. 23. 3D isosurfaces of vortices identified by Q-criterion $Q = 100$ at $t/T_e = 1.56$. (a) $\chi = 0$ and (b) $\chi = 30$.

FIG. 24. 3D isosurfaces of normalized velocity divergence $\vartheta/\vartheta_{rms}$ at t/T_e = 1.56. (a) χ = 0 and (b) χ = 30. Red surfaces: $\vartheta/\vartheta_{rms}$ = −2 and blue surfaces: $\vartheta/\vartheta_{rms}$ = 2.
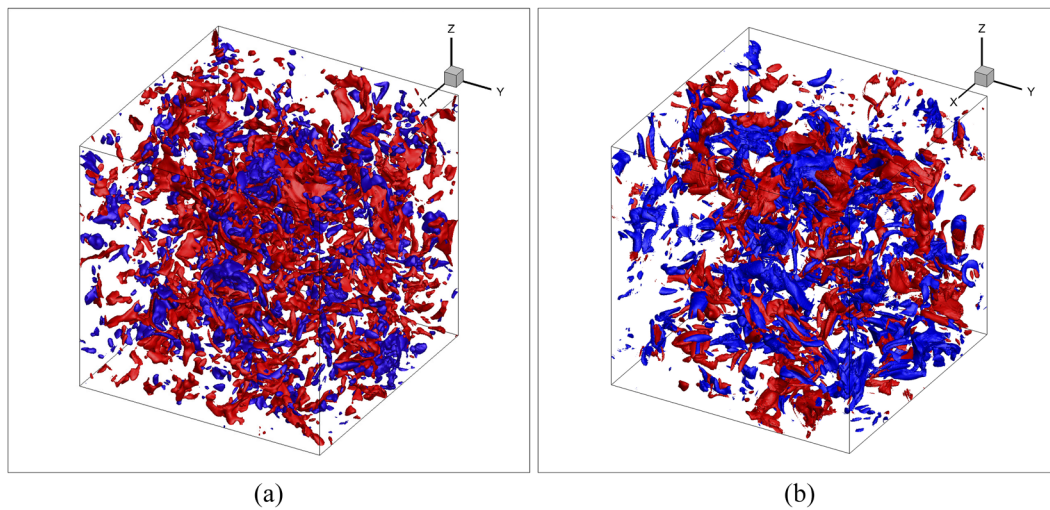
VI. COMPUTATIONAL COST

We ran both the DUGKS code and the hybrid compact FD-WENO code for 10 000 time steps at the 256^3 resolution on the Taiyi cluster provided by the Center for Computational Science and Engineering at the Southern University of Science and Technology. Taiyi is equipped with 815 nodes (2.4 GHz Intel Xeon Gold 614820c), each containing 40 cores. The hybrid compact FD-WENO code was developed by Wang *et al.*[35] and was parallelized using one-dimensional domain decomposition. Due to the requirement to implement the finite difference schemes in the code, the maximum number of the cores that can be used in this case is 64. The total central processing unit (CPU) time is 506 469 s, and the wall clock time is 7 888 s. Our DUGKS code, which was parallelized using the two-dimensional domain decomposition strategy,[52] can be run easily with 256 cores with 16 divisions in each of the two directions (more processors can be used if needed). The total CPU time is 16 658 809 s, and the wall clock time is 65 890 s.

This comparison indicates that currently the DUGKS code is inefficient when compared to the hybrid compact FD-WENO code. Two main reasons are given here. First, the compressible DUGKS code has not been optimized, and many implementation details could be improved. Second, the hybrid compact FD-WENO code only solves five hydrodynamic variables including density (ρ), temperature (T), and three velocity components (u_x, u_y, u_z). While in the DUGKS code, we track the particle distribution functions $\tilde{g}$ and $\tilde{h}$. The hydrodynamic variables are obtained by integrating $\tilde{g}$ and $\tilde{h}$ over the particle velocity space. Using the $E3Q77A9$ discrete particle velocity model, 154 discrete distribution functions were solved, namely, $\tilde{g}_\alpha$ and $\tilde{h}_\alpha$, $\alpha = 1, 2, \ldots, 77$. The relative ratio of the number of variables between the two methods is about 1:30, which reflects roughly the CPU time ratio. We are in the process of optimizing the DUGKS code including decreasing the number of the discrete particle velocities, but such efforts are beyond the scope of the current paper, and they will be reported in the future. The results from the

current paper will serve as a benchmark for such future optimization efforts.

VII. CONCLUSIONS AND DISCUSSIONS

We have proposed a new kinetic model with both an adjustable Prandtl number and a tunable ratio of bulk to shear viscosity and applied the model to simulate CDHIT under the DUGKS approach. Different fifth-order WENO schemes are used to reconstruct the distribution function at the interface, and different treatments of the interfacial derivatives are implemented. Simulation results from various implementations are compared with each other and with the literature data. A newly developed 3D lattice velocity model with 77 discrete particle velocities and a Gauss–Hermite quadrature order at 9 has been used to evaluate the velocity moments of the particle distribution functions. This new lattice velocity model can ensure an accurate evaluation of the heat flux at the mesoscopic level.

We apply the re-designed DUGKS approach to simulate two CDHIT cases with different initial turbulent Mach numbers and Taylor microscale Reynolds numbers. The simulation results agree well with the results from the literature. For the local flow region with high compressible effects, the NSF system may no longer be accurate in describing the local flow state, while the Boltzmann equation can handle both the continuum flow regime and the flows in the non-continuum regimes. Due to the coupled treatment of the particle transport and collision processes, the DUGKS can successfully simulate the flows with multiscale physics, with a second-order accuracy in both space and time. The hydrodynamic variables represent only the low-order moments of the distribution functions. Although the use of more discrete velocities increases the computational cost, more information can be obtained from the particle distribution functions at a given point in the DUGKS.

As a direct application of our DNS data, we study the effect of bulk viscosity on turbulence statistics and structures. The DUGKS

results show that the compressibility effect in CDHIT could be damped with the increase in the bulk to shear viscosity ratio, similar to what has been found in compressible stationary HIT.[37,50]

Our results show that the DUGKS approach can be a reliable tool for simulating CDHIT at low and moderate turbulent Mach numbers. In a companion paper, we first report results in applying the DUGKS approach to simulate compressible stationary HIT.[53] More parametric studies and the code optimization are needed in the future.

APPENDIX A: HERMITE POLYNOMIALS, HERMITE EXPANSION, AND 3D DISCRETE PARTICLE VELOCITY MODEL

The nth order Hermite polynomial[54] is defined by

$$\mathscr{H}^{(n)}(\boldsymbol{\xi}, T_0) \equiv \left(\sqrt{RT_0}\right)^n \frac{(-1)^n}{\omega(\boldsymbol{\xi}, T_0)} \underbrace{\nabla_\xi \cdots \nabla_\xi}_{n-fold} \omega(\boldsymbol{\xi}, T_0), \qquad (A1)$$

where the weighting function $\omega(\boldsymbol{\xi}, T_0)$ is $\omega(\boldsymbol{\xi}, T_0) = \exp(-\xi^2/(2RT_0))/(2\pi RT_0)^{D/2}$ and T_0 is the reference temperature. The Hermite polynomials of different orders are orthogonal to each other in the following sense:

$$\int \omega(\boldsymbol{\xi}, T_0) \mathscr{H}_i^m(\boldsymbol{\xi}, T_0) \mathscr{H}_j^n(\boldsymbol{\xi}, T_0) d\boldsymbol{\xi} = \delta_{mn} \delta_{ij}^n, \qquad (A2)$$

where $\boldsymbol{i}$ represents the abbreviation of $i_1 i_2 \cdots i_n$ and δ_{ij}^n is equal to 1 if and only if $\boldsymbol{i}$ is the permutation of $\boldsymbol{j}$.

From the Chapman–Enskog expansion, we observe that the fourth-order Hermite expansion of the equilibrium g^{eq} and the second-order Hermite expansion of the equilibrium h^{eq} are sufficient for accurate calculation of the heat flux. They are given by

$$g^{eq,N=4} = \rho \omega(\boldsymbol{\xi}, T_0)[A_0 + A_1 + A_2 + A_3 + A_4], \qquad (A3)$$

$$h^{eq,N=2} = (3 - D + K) RT \rho \omega(\boldsymbol{\xi}, T_0)[A_0 + A_1 + A_2], \qquad (A4)$$

where A_0–A_4 are given by

$$A_0 = 1, \quad A_1 = \frac{\boldsymbol{\xi} \cdot \boldsymbol{u}}{RT_0},$$

$$A_2 = \frac{1}{2}\left[\left(\frac{\boldsymbol{\xi} \cdot \boldsymbol{u}}{RT_0}\right)^2 - \frac{u^2}{RT_0} + \left(\frac{T}{T_0} - 1\right)\left(\frac{\xi^2}{RT_0} - D\right)\right],$$

$$A_3 = \frac{1}{6}\left(\frac{\boldsymbol{\xi} \cdot \boldsymbol{u}}{RT_0}\right)\left[\left(\frac{\boldsymbol{\xi} \cdot \boldsymbol{u}}{RT_0}\right)^2 - 3\frac{u^2}{RT_0} + 3\left(\frac{T}{T_0} - 1\right)\left(\frac{\xi^2}{RT_0} - D - 2\right)\right],$$

$$A_4 = \frac{1}{24}\left\{ \begin{array}{l} \left(\frac{\boldsymbol{\xi} \cdot \boldsymbol{u}}{RT_0}\right)^4 - 6\left(\frac{u^2}{RT_0}\right)\left(\frac{\boldsymbol{\xi} \cdot \boldsymbol{u}}{RT_0}\right)^2 + 3\left(\frac{u^2}{RT_0}\right)^2 + 6\left(\frac{T}{T_0} - 1\right) \\ \times \left[\left(\frac{\xi^2}{RT_0} - D - 4\right)\left(\frac{\boldsymbol{\xi} \cdot \boldsymbol{u}}{RT_0}\right)^2 + \frac{u^2}{RT_0}\left(D + 2 - \frac{\xi^2}{RT_0}\right)\right] \\ + 3\left(\frac{T}{T_0} - 1\right)^2\left[\left(\frac{\xi^2}{RT_0}\right)^2 - 2(D+2)\frac{\xi^2}{RT_0} + D(D+2)\right] \end{array} \right\}. \qquad (A5)$$

Based on the orthogonal property of Hermite polynomials, Shan et al.[55,56] developed a general solution of the discrete velocity model by solving linear equations for weights of velocities with predefined abscissas on the lattice points. The three-dimensional discrete velocity model $E_{3,103}^9$ with 103 dicrete particle velocities and a Gauss–Hermite quadrature order at 9 has been proposed. However, the DUGKS does not require the abscissas of the discrete velocities to be coincided with the Cartesian grids. This provides us with an opportunity to design a discrete velocity model with a less number of discrete velocities and the same Gauss–Hermite quadrature order of 9. Recently, a new model $E_{3,77}^9$ with a less number of discrete velocities is proposed by Wen et al.[57] They began with a construction based on $E_{3,125}^9 = E_{1,5}^9 \times E_{1,5}^9 \times E_{1,5}^9$ and then examined the true number of constraints in the model for achieving a Gauss–Hermite quadrature order of 9 in 3D. They found that the one lattice velocity group in $E_{3,125}^9$ can be removed, leading to $E_{3,77}^9$. The relevant symmetry groups, discrete velocity vectors, number of velocities, and the corresponding weights of the resulting $E_{3,77}^9$ model are summarized in Table I, where $r^2 = 5 + \sqrt{10}$, $s^2 = 5 - \sqrt{10}$ are the constants in the discrete velocity vectors.

TABLE I. E3Q77 discrete particle velocity model with ninth-order Gauss–Hermite quadrature.

Group	Vector	Number	Weights
1	$(0, 0, 0)$	1	$1.214\,814\,8 \times 10^{-1}$
2	$(r, 0, 0)$	6	$9.194\,665\,0 \times 10^{-4}$
3	$(s, 0, 0)$	6	$8.056\,201\,5 \times 10^{-2}$
4	$(r, r, 0)$	12	$4.224\,310\,3 \times 10^{-5}$
5	$(s, s, 0)$	12	$1.643\,923\,8 \times 10^{-2}$
6	$(r, s, 0)$	24	$2.499\,999\,9 \times 10^{-3}$
7	(r, r, r)	8	$4.224\,310\,3 \times 10^{-5}$
8	(s, s, s)	8	$1.643\,923\,8 \times 10^{-2}$

APPENDIX B: FIFTH-ORDER WENO SCHEME FOR RECONSTRUCTION OF DISTRIBUTION FUNCTIONS AT CELL INTERFACE

To improve the spatial accuracy, we employ the fifth-order WENO-JS[40] scheme to reconstruct the particle distribution functions at the cell interface. Due to the nature of linear convection of the Boltzmann equation, the upwind rule should be satisfied by considering the directions of particle velocities in order to enhance the numerical stability.

For instance, consider the cell interfaces of which the normal vectors are pointing in the positive x direction. If the x component of the particle velocity $\xi_{\alpha x} > 0$ at the cell interface $x_{j+1/2}$, then by using the third-order interpolation, we can obtain

$$\bar{\phi}^{+(0)}\left(x_{j+1/2}, \boldsymbol{\xi}_\alpha, t_n\right) = \frac{1}{3}\bar{\phi}_{j-2}^{+,n}(\boldsymbol{\xi}_\alpha) - \frac{7}{6}\bar{\phi}_{j-1}^{+,n}(\boldsymbol{\xi}_\alpha) + \frac{11}{6}\bar{\phi}_{j}^{+,n}(\boldsymbol{\xi}_\alpha),$$ (B1a)

$$\bar{\phi}^{+(1)}\left(x_{j+1/2}, \boldsymbol{\xi}_\alpha, t_n\right) = -\frac{1}{6}\bar{\phi}_{j-1}^{+,n}(\boldsymbol{\xi}_\alpha) + \frac{5}{6}\bar{\phi}_{j}^{+,n}(\boldsymbol{\xi}_\alpha) + \frac{1}{3}\bar{\phi}_{j+1}^{+,n}(\boldsymbol{\xi}_\alpha),$$ (B1b)

$$\bar{\phi}^{+(2)}\left(x_{j+1/2}, \boldsymbol{\xi}_\alpha, t_n\right) = \frac{1}{3}\bar{\phi}_{j}^{+,n}(\boldsymbol{\xi}_\alpha) + \frac{5}{6}\bar{\phi}_{j+1}^{+,n}(\boldsymbol{\xi}_\alpha) - \frac{1}{6}\bar{\phi}_{j+2}^{+,n}(\boldsymbol{\xi}_\alpha).$$ (B1c)

It should be noted that the left-hand sides of the above equation are local values at the interface, while the values on the right-hand sides are all cell-averaged.

The smoothness factors β_0, β_1, and β_2 can be explicitly expressed as

$$\beta_0 = \frac{13}{12}\left(\bar{\phi}_{j-2}^{+,n}(\boldsymbol{\xi}_\alpha) - 2\bar{\phi}_{j-1}^{+,n}(\boldsymbol{\xi}_\alpha) + \bar{\phi}_{j}^{+,n}(\boldsymbol{\xi}_\alpha)\right)^2$$
$$+ \frac{1}{4}\left(\bar{\phi}_{j-2}^{+,n}(\boldsymbol{\xi}_\alpha) - 4\bar{\phi}_{j-1}^{+,n}(\boldsymbol{\xi}_\alpha) + 3\bar{\phi}_{j}^{+,n}(\boldsymbol{\xi}_\alpha)\right)^2,$$ (B2a)

$$\beta_1 = \frac{13}{12}\left(\bar{\phi}_{j-1}^{+,n}(\boldsymbol{\xi}_\alpha) - 2\bar{\phi}_{j}^{+,n}(\boldsymbol{\xi}_\alpha) + \bar{\phi}_{j+1}^{+,n}(\boldsymbol{\xi}_\alpha)\right)^2$$
$$+ \frac{1}{4}\left(\bar{\phi}_{j-1}^{+,n}(\boldsymbol{\xi}_\alpha) - \bar{\phi}_{j+1}^{+,n}(\boldsymbol{\xi}_\alpha)\right)^2,$$ (B2b)

$$\beta_2 = \frac{13}{12}\left(\bar{\phi}_{j}^{+,n}(\boldsymbol{\xi}_\alpha) - 2\bar{\phi}_{j+1}^{+,n}(\boldsymbol{\xi}_\alpha) + \bar{\phi}_{j+2}^{+,n}(\boldsymbol{\xi}_\alpha)\right)^2$$
$$+ \frac{1}{4}\left(3\bar{\phi}_{j}^{+,n}(\boldsymbol{\xi}_\alpha) - 4\bar{\phi}_{j+1}^{+,n}(\boldsymbol{\xi}_\alpha) + \bar{\phi}_{j+2}^{+,n}(\boldsymbol{\xi}_\alpha)\right)^2.$$ (B2c)

Therefore, the nonlinear weights can be expressed as

$$\omega_j^{JS} = \frac{\tilde{\omega}_j^{JS}}{\sum_{q=0}^{2}\tilde{\omega}_q^{JS}}, \quad \tilde{\omega}_q^{JS} = \frac{\gamma_q}{(\epsilon_0 + \beta_q)^2}, \, j, q = 0, 1, 2,$$ (B3)

where $\gamma_0 = 1/10$, $\gamma_1 = 3/5$, and $\gamma_2 = 3/10$ are the linear weights. The small parameter ε_0 is originally used to avoid divisions by zero in the nonlinear weights. As suggested, $\varepsilon_0 = 10^{-6}$ is often used in the simulation.[38,40] However, it also has a collateral effect on the order of accuracy of the scheme.[58–60] Therefore, according to the above discussion, ε_0 should be the order of $O\left((\delta x/L)^2\right)$ (with the same dimension as the smoothness factors), where δx is the grid spacing and L is the side length of the cubic box.

Finally, the distribution functions $\bar{\phi}^{+}\left(x_{j+1/2}, \boldsymbol{\xi}_\alpha, t_n\right)$ can be a weighted sum, given as

$$\bar{\phi}^{+}\left(x_{j+1/2}, \boldsymbol{\xi}_\alpha, t_n\right) = \omega_0\bar{\phi}^{+(0)}\left(x_{j+1/2}, \boldsymbol{\xi}_\alpha, t_n\right) + \omega_1\bar{\phi}^{+(1)}\left(x_{j+1/2}, \boldsymbol{\xi}_\alpha, t_n\right)$$
$$+ \omega_2\bar{\phi}^{+(2)}\left(x_{j+1/2}, \boldsymbol{\xi}_\alpha, t_n\right).$$ (B4)

If the x component of the particle velocity $\xi_{\alpha x} < 0$ at the cell interface $x_{j+1/2}$, the similar procedures can be repeated with three cells in the upstream direction and two cells in the downstream direction. If $\xi_{\alpha x} = 0$, we take the average of the results obtained by two cases mentioned above. For the cell interfaces in the y direction and z direction, the logic is similar to what we have done in the x direction. The reconstruction process is displayed in Fig. 25.

The WENO-JS scheme can lose its optimal order of accuracy at the critical points (where $df/dx = 0$, but $d^2f/dx^2 \neq 0$) of a smooth function.[41,59] Therefore, Borges et al.[41] and Castro et al.[42] proposed the WENO-Z scheme by redesigning the nonlinear weights that satisfy the necessary and sufficient conditions for an optimal order at the critical points. The WENO-Z scheme is less dissipative than WENO-JS.[60] In addition to WENO-JS and WENO-Z schemes, Henrick et al.[43] proposed the WENO-M scheme by introducing a mapping function to the weights. The above conclusions are drawn from 1D or 2D simulations in the existing literature. For the present 3D implementation using the DUGKS approach, the effect of different WENO schemes on turbulence statistics should also be further studied.
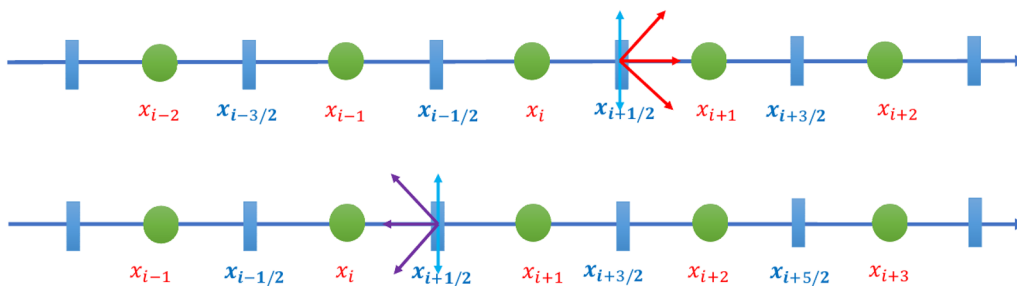

FIG. 25. The fifth-order WENO scheme for the reconstruction of particle distribution functions at the cell interface.

APPENDIX C: CHAPMAN–ENSKOG ANALYSIS FOR THE REDESIGNED MESOSCOPIC MODEL

In this appendix, we provide the details of the Chapman–Enskog analysis for the redesigned mesoscopic model. From Eqs. (8a) and (8b), the Chapman–Enskog expansion for two reduced distribution functions g and h can be written as

$$g = g^{eq} - \tau\left(\frac{\partial g^{eq}}{\partial t} + \boldsymbol{\xi} \cdot \nabla g^{eq} - S_g\right) + O(\tau^2), \qquad \text{(C1a)}$$

$$h = h^{eq} - \tau\left(\frac{\partial h^{eq}}{\partial t} + \boldsymbol{\xi} \cdot \nabla h^{eq} - S_h\right) + O(\tau^2). \qquad \text{(C1b)}$$

From the definitions of the equilibriums and source terms in Eqs. (9) and (10), the following moments can be evaluated directly:

$$\int g^{eq}d\boldsymbol{\xi} = \rho, \quad \int \boldsymbol{\xi}g^{eq}d\boldsymbol{\xi} = \rho\boldsymbol{u}, \quad \int (\xi^2 g^{eq} + h^{eq})d\boldsymbol{\xi} = 2\rho E, \quad \text{(C2)}$$

$$\int S_g d\boldsymbol{\xi} = 0, \quad \int \boldsymbol{\xi}S_g d\boldsymbol{\xi} = \boldsymbol{0},$$
$$\int \boldsymbol{\xi\xi}S_g d\boldsymbol{\xi} = -\left(\chi - \frac{2(3-D+K)}{D(3+K)}\right)p\vartheta\boldsymbol{I}, \quad \int \boldsymbol{\xi\xi\xi}S_g d\boldsymbol{\xi} = \boldsymbol{0}, \qquad \text{(C3)}$$

$$\int S_h d\boldsymbol{\xi} = D\left(\chi - \frac{2(3-D+K)}{D(3+K)}\right)p\vartheta,$$
$$\int \boldsymbol{\xi}S_h d\boldsymbol{\xi} = \frac{2(1-Pr)\boldsymbol{q}}{\tau} - 2\left(\chi - \frac{2(3-D+K)}{D(3+K)}\right)p\vartheta\boldsymbol{u}. \qquad \text{(C4)}$$

Combination of Eqs. (11) and (C2) yields the conservation requirements for the collision operators,

$$\int \Omega_g d\boldsymbol{\xi} = 0, \quad \int \boldsymbol{\xi}\Omega_g d\boldsymbol{\xi} = \boldsymbol{0}, \quad \int \left(\xi^2\Omega_g + \Omega_h\right)d\boldsymbol{\xi} = 0. \qquad \text{(C5)}$$

Then, by taking the zeroth moment of Eq. (8a), we obtain the continuity equation [see Eq. (14a)]. Similarly, by taking the first-order moment of Eq. (8a), we obtain the momentum equation [see Eq. (14b)]. By using Eq. (C1a), we can obtain the explicit expression for the viscous stress tensor in Eq. (12).

Likewise, by taking the second-order moment of Eq. (8a) and the zeroth-order moment for Eq. (8b), we have

$$\frac{1}{2}\frac{\partial}{\partial t}\int h d\boldsymbol{\xi} + \frac{1}{2}\nabla \cdot \int \boldsymbol{\xi}h d\boldsymbol{\xi} = \frac{1}{2}\int \Omega_h d\boldsymbol{\xi} + \frac{1}{2}\int S_h d\boldsymbol{\xi}, \qquad \text{(C6)}$$

$$\frac{1}{2}\frac{\partial}{\partial t}\int \xi^2 g d\boldsymbol{\xi} + \frac{1}{2}\nabla \cdot \int \xi^2 \boldsymbol{\xi}g d\boldsymbol{\xi} = \frac{1}{2}\int \xi^2\Omega_g d\boldsymbol{\xi} + \frac{1}{2}\int \xi^2 S_g d\boldsymbol{\xi}. \qquad \text{(C7)}$$

The sum of Eqs. (C6) and (C7) gives the total energy equation in Eq. (14c).

The remaining task is to find the explicit expression for the heat flux $\boldsymbol{q}$ by using the Chapman–Enskog expansion of two reduced distribution functions given in Eqs. (C1a) and (C1b). First, we note that by using Eqs. (C3) and (C4), we obtain

$$\int \boldsymbol{c}c^2 S_g d\boldsymbol{\xi} = (D+2)\left(\chi - \frac{2(3-D+K)}{D(3+K)}\right)p\vartheta\boldsymbol{u}, \qquad \text{(C8a)}$$

$$\int \boldsymbol{c}S_h d\boldsymbol{\xi} = \frac{2(1-Pr)\boldsymbol{q}}{\tau} - (D+2)\left(\chi - \frac{2(3-D+K)}{D(3+K)}\right)p\vartheta\boldsymbol{u}. \quad \text{(C8b)}$$

Therefore, we have

$$\int \boldsymbol{c}(c^2 S_g + S_h)d\boldsymbol{\xi} = \frac{2(1-Pr)\boldsymbol{q}}{\tau}. \qquad \text{(C9)}$$

Using Eq. (C9), the heat flux $\boldsymbol{q}$ can be computed as

$$\begin{aligned}
\boldsymbol{q} &= -\frac{1}{2}\tau\left[\int \boldsymbol{c}c^2\left(\frac{\partial g^{eq}}{\partial t} + \boldsymbol{\xi} \cdot \nabla g^{eq}\right)d\boldsymbol{\xi}\right. \\
&\quad \left. + \int \boldsymbol{c}\left(\frac{\partial h^{eq}}{\partial t} + \boldsymbol{\xi} \cdot \nabla h^{eq}\right)d\boldsymbol{\xi}\right] \\
&\quad + \frac{1}{2}\tau\int \boldsymbol{c}c^2 S_g d\boldsymbol{\xi} + \frac{1}{2}\tau\int \boldsymbol{c}S_h d\boldsymbol{\xi} + \boldsymbol{O}(\tau^2) \\
&= -p\tau c_p\nabla T + \frac{1}{2}\tau\int \boldsymbol{c}(c^2 S_g + S_h)d\boldsymbol{\xi} + \boldsymbol{O}(\tau^2) \\
&= -p\tau c_p\nabla T + (1-Pr)\boldsymbol{q} + \boldsymbol{O}(\tau^2). \qquad \text{(C10)}
\end{aligned}$$

Therefore, the Fourier's law can be recovered, as shown in Eq. (13).

Finally, it is worth pointing out that the source terms can be designed by applying the Hermite expansion with five constraints in order to recover the NSF system.[47] Obviously, the simplest choice is to take a truncated Hermite polynomial without increasing the Gauss–Hermite quadrature order.

APPENDIX D: EXPLICIT EXPRESSIONS OF THE TWO REDUCED DISTRIBUTION FUNCTIONS

The following Euler equations can be easily obtained by approximating the distribution functions by the corresponding equilibriums to the order of $O(1)$:

$$\frac{\partial\rho}{\partial t} + \nabla \cdot (\rho\boldsymbol{u}) = 0, \qquad \text{(D1a)}$$

$$\rho\left(\frac{\partial\boldsymbol{u}}{\partial t} + \boldsymbol{u} \cdot \nabla\boldsymbol{u}\right) = -\nabla p + \boldsymbol{O}(\tau), \qquad \text{(D1b)}$$

$$\rho c_v\left(\frac{\partial T}{\partial t} + \boldsymbol{u} \cdot \nabla T\right) = -p\vartheta + O(\tau). \qquad \text{(D1c)}$$

Similarly, by performing the Chapman–Enskog expansion in the hydrodynamic limit, the particle distribution function can be approximated by its equilibrium and relevant derivatives to the

order of $O(\tau)$. Through direct evaluation, we found that the time derivative and the spatial derivative of the equilibrium distribution function g^{eq} are proportional to itself, and the coefficient includes both the time and spatial derivatives of the hydrodynamic flow variables,

$$\frac{\partial g^{eq}}{\partial t} = \left[\frac{1}{\rho}\frac{\partial \rho}{\partial t} + \left(\frac{c^2}{2RT} - \frac{D}{2}\right)\frac{1}{T}\frac{\partial T}{\partial t} + \frac{\partial \boldsymbol{u}}{\partial t} \cdot \frac{\boldsymbol{c}}{RT}\right]g^{eq}, \quad (D2a)$$

$$\nabla g^{eq} = \left[\frac{1}{\rho}\nabla\rho + \left(\frac{c^2}{2RT} - \frac{D}{2}\right)\frac{1}{T}\nabla T + \nabla \boldsymbol{u} \cdot \frac{\boldsymbol{c}}{RT}\right]g^{eq}. \quad (D2b)$$

If we use the Euler equations [see Eq. (D1)] to replace the time derivatives of the hydrodynamic variables with the spatial derivatives, we can obtain the Chapman–Enskog expansion of the two reduced distribution functions to the order of $O(\tau)$,

$$g = (1 - \tau G)g^{eq} + \tau S_g + O(\tau^2), \quad (D3a)$$

$$h = (1 - \tau G - \tau\Phi_1)h^{eq} + \tau S_h + O(\tau^2), \quad (D3b)$$

where the coefficient $G = G_1 + G_2$ and G_1, G_2, and Φ_1 are given by

$$G_1 = \left(\frac{c^2}{2RT} - \frac{D+2}{2}\right)\boldsymbol{c} \cdot \left(\frac{1}{T}\nabla T\right), \quad (D4a)$$

$$G_2 = \frac{\boldsymbol{c} \cdot \boldsymbol{S} \cdot \boldsymbol{c}}{RT} - \frac{1}{K+3}\left(\frac{c^2}{RT} + 3 - D + K\right)\vartheta, \quad (D4b)$$

$$\Phi_1 = \boldsymbol{c} \cdot \left(\frac{1}{T}\nabla T\right) - \frac{2}{3+K}\vartheta. \quad (D4c)$$

Equations (D3) and (D4) can be used to initialize two reduced distribution functions $\tilde{g}$ and $\tilde{h}$.

APPENDIX E: A DERIVATION OF THE EVOLUTION EQUATION OF MEAN SQUARE VELOCITY DIVERGENCE

Taking the divergence of both sides of Eq. (14b), we obtain

$$\frac{\partial \vartheta}{\partial t} + \boldsymbol{S} : \boldsymbol{S} - \boldsymbol{\Omega} : \boldsymbol{\Omega} + \boldsymbol{u} \cdot \nabla\vartheta = -\nabla \cdot \left(\frac{1}{\rho}\nabla p\right) + \nabla \cdot \left(\frac{1}{\rho}\nabla \cdot \boldsymbol{\sigma}\right), \quad (E1)$$

where $\boldsymbol{\Omega} = (\nabla \boldsymbol{u}^T - \nabla \boldsymbol{u})/2$ is the rotation tensor.

Multiplying Eq. (E1) by the dilatation on both sides and then averaging the resulting equation over the periodic domain, we obtain

$$\frac{\partial}{\partial t}\left\langle\frac{1}{2}\vartheta^2\right\rangle = \left\langle\frac{1}{2}\vartheta^3\right\rangle + \left\langle\vartheta(\boldsymbol{\Omega} : \boldsymbol{\Omega} - \boldsymbol{S} : \boldsymbol{S})\right\rangle + \left\langle\frac{1}{\rho}\nabla p \cdot \nabla\vartheta\right\rangle$$
$$- \left\langle\frac{1}{\rho}\nabla\vartheta \cdot (\nabla \cdot \boldsymbol{\sigma})\right\rangle. \quad (E2)$$

Furthermore, using the identity $\nabla\vartheta \cdot \nabla^2\boldsymbol{u} = \nabla \cdot (\vartheta\nabla^2\boldsymbol{u} - \vartheta\nabla\vartheta) + |\nabla\vartheta|^2$, the viscous term in Eq. (E2) can be evaluated as

$$-\frac{1}{\rho}\nabla\vartheta \cdot (\nabla \cdot \boldsymbol{\sigma}) = -2\frac{1}{\rho}\nabla\mu \cdot \boldsymbol{S}^d \cdot \nabla\vartheta$$
$$- \nabla \cdot \left(\frac{\mu}{\rho}(\vartheta\nabla^2\boldsymbol{u} - \vartheta\nabla\vartheta)\right)$$
$$+ (\vartheta\nabla^2\boldsymbol{u} - \vartheta\nabla\vartheta) \cdot \nabla\nu - \frac{4}{3}\frac{\mu}{\rho}|\nabla\vartheta|^2$$
$$- \frac{1}{\rho}\vartheta\nabla\vartheta \cdot \nabla\mu_V - \frac{\mu_V}{\rho}|\nabla\vartheta|^2, \quad (E3)$$

where $\boldsymbol{S}^d = \boldsymbol{S} - (1/3)\vartheta\boldsymbol{I}$ is the traceless part of the strain rate tensor.

Combining Eqs. (E2) and (E3) gives the evolution equation for $\langle\vartheta^2\rangle/2$,

$$\frac{\partial}{\partial t}\left\langle\frac{1}{2}\vartheta^2\right\rangle = \left\langle\frac{1}{2}\vartheta^3\right\rangle + \left\langle\vartheta(\boldsymbol{\Omega} : \boldsymbol{\Omega} - \boldsymbol{S} : \boldsymbol{S})\right\rangle + \left\langle\frac{1}{\rho}\nabla p \cdot \nabla\vartheta\right\rangle$$
$$- \left\langle 2\frac{1}{\rho}\nabla\mu \cdot \boldsymbol{S}^d \cdot \nabla\vartheta\right\rangle + \left\langle(\vartheta\nabla^2\boldsymbol{u} - \vartheta\nabla\vartheta) \cdot \nabla\nu\right\rangle$$
$$- \left\langle\frac{4}{3}\frac{\mu}{\rho}|\nabla\vartheta|^2\right\rangle - \left\langle\frac{1}{\rho}\vartheta\nabla\vartheta \cdot \nabla\mu_V\right\rangle - \left\langle\frac{\mu_V}{\rho}|\nabla\vartheta|^2\right\rangle, \quad (E4)$$

where on the right-hand side, the first term originates from the advection term, the second term represents the vorticity-dilatation effect, the third term denotes the coupling effect induced by the pressure gradient and dilatation gradient, the sixth term represents the dilatational dissipation due to the shear viscosity and the dilatation gradient, and the eighth term denotes the dilatational dissipation induced by the bulk viscosity. The remaining terms are related to the non-uniform distribution of the shear and bulk viscosities.

If both the shear viscosity gradient and the bulk viscosity gradient are relatively small [for instance, the ratio $(\langle\mu\rangle - \mu_0)/\mu_0 < 5\%$ in our simulations] such that the terms relevant to these gradients can be neglected, then Eq. (E4) can be reduced to Eq. (40).

DATA AVAILABILITY

The data that support the findings of this study are available from the corresponding author upon reasonable request.

REFERENCES

[1] G. Bird, *Molecular Gas Dynamics and the Direct Simulation of Gas Flows* (Clarendon, Oxford, 1994), Vol. 42.

[2] L. Zhu, Z. Guo, and K. Xu, "Discrete unified gas kinetic scheme on unstructured meshes," Comput. Fluids **127**, 211–225 (2016).

[3] Z.-X. Tong, Y.-L. He, and W.-Q. Tao, "A review of current progress in multiscale simulations for fluid flow and heat transfer problems: The frameworks, coupling techniques and future perspectives," Int. J. Heat Mass Transfer **137**, 1263–1289 (2019).

[4] G. A. Bird, "Recent advances and current challenges for DSMC," Comput. Math. Appl. **35**, 1–14 (1998).

[5] J. Fan and C. Shen, "Statistical simulation of low-speed rarefied gas flows," J. Comput. Phys. **167**, 393–412 (2001).

[6] P. Wang, M. T. Ho, L. Wu, Z. Guo, and Y. Zhang, "A comparative study of discrete velocity methods for low-speed rarefied gas flows," Comput. Fluids **161**, 33–46 (2018).

[7] L. M. Yang, C. Shu, J. Wu, and Y. Wang, "Comparative study of discrete velocity method and high-order lattice Boltzmann method for simulation of rarefied flows," Comput. Fluids **146**, 125–142 (2017).

[8] L. Mieussens, "Discrete-velocity models and numerical schemes for the Boltzmann-BGK equation in plane and axisymmetric geometries," J. Comput. Phys. **162**, 429–466 (2000).

[9] A. S. Jebakumar, V. Magi, and J. Abraham, "Lattice-Boltzmann simulations of particle transport in a turbulent channel flow," Int. J. Heat Mass Transfer **127**, 339–348 (2018).

[10] S. Chen and G. D. Doolen, "Lattice Boltzmann method for fluid flows," Annu. Rev. Fluid Mech. **30**, 329–364 (1998).

[11] P. K. Kolluru, M. Atif, M. Namburi, and S. Ansumali, "Lattice Boltzmann model for weakly compressible flows," Phys. Rev. E **101**, 013309 (2020).

[12] K. Xu and J.-C. Huang, "A unified gas-kinetic scheme for continuum and rarefied flows," J. Comput. Phys. **229**, 7747–7764 (2010).

[13] J.-C. Huang, K. Xu, and P. Yu, "A unified gas-kinetic scheme for continuum and rarefied flows II: Multi-dimensional cases," Commun. Comput. Phys. **12**, 662–690 (2012).

[14] J.-C. Huang, K. Xu, and P. Yu, "A unified gas-kinetic scheme for continuum and rarefied flows III: Microflow simulations," Commun. Comput. Phys. **14**, 1147–1173 (2013).

[15] C. Liu, K. Xu, Q. Sun, and Q. Cai, "A unified gas-kinetic scheme for continuum and rarefied flows IV: Full Boltzmann and model equations," J. Comput. Phys. **314**, 305–340 (2016).

[16] K. Xu, "A gas-kinetic BGK scheme for the Navier–Stokes equations and its connection with artificial dissipation and Godunov method," J. Comput. Phys. **171**, 289–335 (2001).

[17] Z. Guo, K. Xu, and R. Wang, "Discrete unified gas kinetic scheme for all Knudsen number flows: Low-speed isothermal case," Phys. Rev. E **88**, 033305 (2013).

[18] Z. Guo, K. Xu, and R. Wang, "Discrete unified gas kinetic scheme for all Knudsen number flows. II. Thermal compressible case," Phys. Rev. E **91**, 033313 (2015).

[19] P. Wang, L.-P. Wang, and Z. Guo, "Comparison of the lattice Boltzmann equation and discrete unified gas-kinetic scheme methods for direct numerical simulation of decaying turbulent flows," Phys. Rev. E **94**, 043304 (2016).

[20] Y. Bo, P. Wang, Z. Guo, and L.-P. Wang, "DUGKS simulations of three-dimensional Taylor-Green vortex flow and turbulent channel flow," Comput. Fluids **155**, 9–21 (2017).

[21] C. Wu, B. Shi, Z. Chai, and P. Wang, "Discrete unified gas kinetic scheme with a force term for incompressible fluid flows," Comput. Math. Appl. **71**, 2608–2629 (2016).

[22] H. Liu, Y. Cao, Q. Chen, M. Kong, and L. Zheng, "A conserved discrete unified gas kinetic scheme for microchannel gas flows in all flow regimes," Comput. Fluids **167**, 313–323 (2018).

[23] Z. Yang, C. Zhong, and C. Zhuo, "Phase-field method based on discrete unified gas-kinetic scheme for large-density-ratio two-phase flows," Phys. Rev. E **99**, 043302 (2019).

[24] C. Zhang, K. Yang, and Z. Guo, "A discrete unified gas-kinetic scheme for immiscible two-phase flows," Int. J. Heat Mass Transfer **126**, 1326–1336 (2018).

[25] H. Liu, M. Kong, Q. Chen, L. Zheng, and Y. Cao, "Coupled discrete unified gas kinetic scheme for the thermal compressible flows in all Knudsen number regimes," Phys. Rev. E **98**, 053310 (2018).

[26] Z. Guo, C. Zheng, B. Shi, and T. Zhao, "Thermal lattice Boltzmann equation for low Mach number flows: Decoupling model," Phys. Rev. E **75**, 036704 (2007).

[27] J. Chen, S. Liu, Y. Wang, and C. Zhong, "Conserved discrete unified gas-kinetic scheme with unstructured discrete velocity space," Phys. Rev. E **100**, 043305 (2019).

[28] R. Yuan and C. Zhong, "A conservative implicit scheme for steady state solutions of diatomic gas flow in all flow regimes," Comput. Phys. Commun. **247**, 106972 (2020).

[29] R. Samtaney, D. I. Pullin, and B. Kosović, "Direct numerical simulation of decaying compressible turbulence and shocklet statistics," Phys. Fluids **13**, 1415–1430 (2001).

[30] A. E. Honein and P. Moin, "Higher entropy conservation and numerical stability of compressible turbulence simulations," J. Comput. Phys. **201**, 531–545 (2004).

[31] N. Frapolli, S. S. Chikatamarla, and I. V. Karlin, "Entropic lattice Boltzmann model for compressible flows," Phys. Rev. E **92**, 061301 (2015).

[32] W. Liao, Y. Peng, and L.-S. Luo, "Gas-kinetic schemes for direct numerical simulations of compressible homogeneous turbulence," Phys. Rev. E **80**, 046702 (2009).

[33] P. K. Subbareddy and G. V. Candler, "A fully discrete, kinetic energy consistent finite-volume scheme for compressible flows," J. Comput. Phys. **228**, 1347–1364 (2009).

[34] F. Ducros, V. Ferrand, F. Nicoud, C. Weber, D. Darracq, C. Gacherieu, and T. Poinsot, "Large-eddy simulation of the shock/turbulence interaction," J. Comput. Phys. **152**, 517–549 (1999).

[35] J. Wang, L.-P. Wang, Z. Xiao, Y. Shi, and S. Chen, "A hybrid numerical simulation of isotropic compressible turbulence," J. Comput. Phys. **229**, 5257–5279 (2010).

[36] L. Liu, J. Wang, Y. Shi, S. Chen, and X. He, "A hybrid numerical simulation of supersonic isotropic turbulence," Commun. Comput. Phys. **25**, 189–217 (2019).

[37] S. Chen, X. Wang, J. Wang, M. Wan, H. Li, and S. Chen, "Effects of bulk viscosity on compressible homogeneous turbulence," Phys. Fluids **31**, 085115 (2019).

[38] G. Cao, L. Pan, and K. Xu, "Three dimensional high-order gas-kinetic scheme for supersonic isotropic turbulence I: Criterion for direct numerical simulation," Comput. Fluids **192**, 104273 (2019).

[39] S. Küchlin and P. Jenny, "Parallel Fokker-Planck-DSMC algorithm for rarefied gas flow simulation in complex domains at all Knudsen numbers," J. Comput. Phys. **328**, 258–277 (2017).

[40] G.-S. Jiang and C.-W. Shu, "Efficient implementation of weighted ENO schemes," J. Comput. Phys. **126**, 202–228 (1996).

[41] R. Borges, M. Carmona, B. Costa, and W. S. Don, "An improved weighted essentially non-oscillatory scheme for hyperbolic conservation laws," J. Comput. Phys. **227**, 3191–3211 (2008).

[42] M. Castro, B. Costa, and W. S. Don, "High order weighted essentially non-oscillatory WENO-Z schemes for hyperbolic conservation laws," J. Comput. Phys. **230**, 1766–1792 (2011).

[43] A. K. Henrick, T. D. Aslam, and J. M. Powers, "Mapped weighted essentially non-oscillatory schemes: Achieving optimal order near critical points," J. Comput. Phys. **207**, 542–567 (2005).

[44] S. Chapman and T. G. Cowling, *The Mathematical Theory of Non-Uniform Gases* (Cambridge University Press, 1952).

[45] E. Shakhov, "Generalization of the Krook kinetic relaxation equation," Fluid Dyn. **3**, 95–96 (1972).

[46] W. Sutherland, "The viscosity of gases and molecular force," Philos. Mag. **36**, 507–531 (1893).

[47] T. Chen, L.-P. Wang, J. Lai, and S. Chen, "Inverse design of mesoscopic models for compressible flow using the Chapman-Enskog analysis," Adv. Aerodyn. (submitted).

[48] B. van Leer, "Towards the ultimate conservative difference scheme. IV. A new approach to numerical convection," J. Comput. Phys. **23**, 276–299 (1977).

[49] Z. Guo and C. Zheng, *Theory and Applications of Lattice Boltzmann Method* (Science Press, China, 2009).

[50] S. Pan and E. Johnsen, "The role of bulk viscosity on the decay of compressible, homogeneous, isotropic turbulence," J. Fluid Mech. **833**, 717–744 (2017).

[51] J. Jeong and F. Hussain, "On the identification of a vortex," J. Fluid Mech. **285**, 69–94 (1995).

[52] N. Geneva, C. Peng, X. Li, and L.-P. Wang, "A scalable interface-resolved simulation of particle-laden flow using the lattice Boltzmann method," Parallel Comput. **67**, 20–37 (2017).

[53]T. Chen, X. Wen, L.-P. Wang, Z. Guo, J. Wang, and S. Chen, "Simulation of three-dimensional forced compressible isotropic turbulence by a redesigned discrete unified gas kinetic scheme," J. Comput. Phys. (submitted) (2020).

[54]H. Grad, "Note on N-dimensional Hermite polynomials," Commun. Pure Appl. Math. **2**, 325–330 (1949).

[55]X. Shan, X.-F. Yuan, and H. Chen, "Kinetic theory representation of hydrodynamics: A way beyond the Navier-Stokes equation," J. Fluid Mech. **550**, 413–441 (2006).

[56]X. Shan, "General solution of lattices for Cartesian lattice Bhatanagar-Gross-Krook models," Phys. Rev. E **81**, 036702 (2010).

[57]X. Wen, L.-P. Wang, and Z. Guo, "Simulation of compressible natural convection flows using an improved discrete unified gas kinetic scheme," Int. J. Heat Mass Transfer (submitted) (2020).

[58]N. K. Yamaleev and M. H. Carpenter, "Third-order energy stable WENO scheme," J. Comput. Phys. **228**, 3025–3047 (2009).

[59]W.-S. Don and R. Borges, "Accuracy of the weighted essentially non-oscillatory conservative finite difference schemes," J. Comput. Phys. **250**, 347–372 (2013).

[60]F. Acker, R. B. d. R. Borges, and B. Costa, "An improved WENO-Z scheme," J. Comput. Phys. **313**, 726–753 (2016).